



Scaling behaviour of rotating convection in a spherical shell with different Prandtl numbers

Wei Fan¹, Qi Wang¹ and Yufeng Lin^{1,2,†}

¹Department of Earth and Space Sciences, Southern University of Science and Technology, Shenzhen 518055, PR China

²Center for Complex Flows and Soft Matter Research, Southern University of Science and Technology, Shenzhen 518055, PR China

(Received 20 March 2024; revised 3 September 2024; accepted 4 September 2024)

Rayleigh–Bénard convection in a rotating spherical shell provides a simplified model for convective dynamics of planetary and stellar interiors. Over the past decades, the problem has been studied extensively via numerical simulations, but most previous simulations set the Prandtl number Pr to unity. In this study we build more than 200 numerical models of rotating convection in a spherical shell over a wide range of Pr ($10^{-2} \leq Pr \leq 10^2$). By increasing the Rayleigh number Ra , we characterise four different flow regimes, starting from the linear onset to multiple modes, then transitioning to the geostrophic turbulence and eventually approaching the weakly rotating regime. In the multiple modes regime, we show evidence of triadic resonances in numerical models with different Pr , which may provide a generic mechanism for the transition from laminar to turbulence in rotating convection. We analyse scaling behaviours of the heat transfer and convective flow speeds in numerical simulations, paying particular attention to the Pr dependence. We find that the so-called diffusion-free scaling for the heat transfer cannot reconcile all numerical models with different Pr in the geostrophic turbulence regime. However, the characteristic flow speeds at different Pr roughly follow a unified scaling that can be described by visco-Archimedean–Coriolis force balances, though the scaling tends to approach the Coriolis-inertial-Archimedean force balance at low Pr . We also show that transition behaviours from rotating to non-rotating convection depend on Pr . The transition criteria based on heat transfer and flow morphology would be rather different when $Pr > 1$, but the two criteria are consistent for cases with $Pr \leq 1$. Both scaling behaviours and transition behaviours suggest that the heat transfer is controlled by the boundary layers while the convective flow speeds are mainly determined by the force balance in the bulk for cases with $Pr > 1$, which is in line with recent experimental results with moderate to high Pr . For cases with $Pr \leq 1$, both the heat transfer and convective velocities are approaching the inviscid dynamics in the bulk. We also briefly analysed the

† Email address for correspondence: linyf@sustech.edu.cn

magnitude and scaling of zonal flows at different Pr , showing that the zonal flow amplitude rapidly increases as Pr decreases.

Key words: Bénard convection, buoyancy-driven instability, rotating turbulence

1. Introduction

Rotation plays an important role in many natural convection systems such as Earth's liquid outer core, convective envelopes of giant planets and rotating stars (Aurnou *et al.* 2015; Jones 2015). Rotating Rayleigh–Bénard convection (RRBC) provides a canonical model for studying convective dynamics under the influence of rotation (Chandrasekhar 1961). The RRBC problem has been extensively studied for many decades using theoretical analysis, numerical simulations and laboratory experiments (e.g. see review articles Ecke & Shishkina 2023; Xia *et al.* 2023). While the RRBC model captures some aspects of the key dynamics of rotating convection in a local region, it is important to consider the effect of spherical geometry for the global dynamics of planetary and stellar interiors.

Theoretical works on spherical rotating convection concentrated on the onset of convection (Chandrasekhar 1961; Roberts 1968; Busse 1970; Zhang 1994; Jones, Soward & Mussa 2000; Dormy *et al.* 2004). A few experiments were conducted to model spherical rotating convection using centrifugal gravity (e.g. Busse & Carrigan 1976; Cardin & Olson 1994; Aubert *et al.* 2001), but it is difficult to explore a wide range of parameter regimes due to practical considerations. The spherical rotating convection in the highly supercritical regime has been mainly studied using direct numerical simulations (e.g. Gilman 1977; Tilgner & Busse 1997; Christensen 2002; Gillet & Jones 2006; Aurnou, Heimpel & Wicht 2007; Yadav *et al.* 2016; Guervilly, Cardin & Schaeffer 2019). Several scaling laws of rotating convection have been proposed based on heuristic arguments (Stevenson 1979; Aurnou, Horn & Julien 2020) and tested using numerical models in spherical geometries (Gastine, Wicht & Aubert 2016; Long *et al.* 2020; Lin & Jackson 2021). However, most previous simulations set Pr to unity, which may mask some scaling behaviours depending on Pr . It is important to consider the Pr dependence when extrapolating scaling laws to planetary cores because thermal and compositional diffusivities are different in planetary core conditions (Li *et al.* 2000; Labrosse 2003; Zhang *et al.* 2020*b*), corresponding to quite different Pr for thermal convection ($Pr \sim 0.01$) and compositional convection ($Pr \sim 10$). In this study we perform a set of numerical simulations of rotating convection in a spherical shell over a wide range of Pr ($10^{-2} \leq Pr \leq 10^2$).

There are two branches of rotating convection near the onset depending on Pr , namely viscous convection and inertial convection (Zhang & Liao 2017). At large Pr ($Pr \geq 1$), the onset of convection invokes the viscous force and is in the form of quasi-steady columnar rolls (Busse 1970; Jones *et al.* 2000). The critical Rayleigh number for the viscous convection scales as $Ra_c \sim E^{-4/3}$, and the azimuthal wavenumber of the onset (ON) mode $m_c \sim E^{-1/3}$, where E is the Ekman number. At low Pr ($Pr \ll 1$), the onset of convection invokes the inertial term and is in the form of oscillatory inertial modes (Zhang 1994). The critical Rayleigh number for the inertial convection scales as $Ra_c \sim E^{-1/2}$ and the azimuthal wavenumber of the ON mode $m_c \sim O(1)$ (Zhang & Liao 2017). Of course, there always exists a transition from viscous convection to inertial convection depending on E and Pr , where the onset is characterised by spiralling columnar convection (Zhang 1992). More recently, it has been found that the subcritical convection can occur at low Pr

(Guervilly & Cardin 2016; Kaplan *et al.* 2017). These findings highlighted the significant role of Pr in rotating convection near the onset.

In the highly supercritical regime, the rigorous theoretical analysis is not tractable. Nevertheless, some scaling laws regarding the heat transfer efficiency, the typical convective flow speed and length scale have been proposed relying on heuristic arguments and force balances (Stevenson 1979; Aubert *et al.* 2001; Gillet & Jones 2006; Barker, Dempsey & Lithwick 2014; Aurnou *et al.* 2020). For rotating turbulent convection, which is the most relevant regime to the planetary core dynamics, the so-called diffusion-free scalings or inertial scalings have been widely used to compare experimental and numerical results (Cheng *et al.* 2018; Hawkins *et al.* 2023). The diffusion-free scalings were derived using various approaches in the literature, but these scalings are essentially based on the Coriolis-inertial-Archimedean (CIA) force balance and incorporated with the mixing length theory, leading to scalings independent of the fluid viscosity and thermal diffusivity (Stevenson 1979; Julien *et al.* 2012; Jones 2015). The diffusion-free scalings predict the heat transfer efficiency measured by the Nusselt number $Nu \sim Ra^{3/2}E^2Pr^{-1/2}$, and the convective flow speed measured by the non-zonal Reynolds number $Re_{non} \sim (Ra_QPr^{-2}E^{1/2})^{2/5}$, where Ra_Q is the flux-based Rayleigh number $Ra_Q = (Nu - 1)Ra$. These scalings exhibit Pr dependence, but most previous numerical studies mainly considered the dependence on Ra and E . These scalings were tested using direct numerical simulations over a wide range of Ra and E in rotating spherical shells with the fixed temperature (Gastine *et al.* 2016) and fixed-flux (Long *et al.* 2020) boundary conditions, and in a uniformly heated full sphere (Lin & Jackson 2021). More recently, Wang *et al.* (2021), Gastine & Aurnou (2023) examined the latitudinal dependence of the heat transfer in rotating spherical shells. Gastine & Aurnou (2023) found that the heat transfer scaling in the polar region is steeper than the diffusion-free scaling, whereas the scaling in the equatorial region is less steep than the diffusion-free scaling. Wang *et al.* (2021) showed that the diffusion-free scalings may be valid in the mid-latitude flow region. Note that some recent studies in cylindrical domains also reveal that the heat transfer scaling has a radius dependence due to the difference between bulk convective flow and sidewall dynamics (de Wit *et al.* 2020; Zhang *et al.* 2020a; Zhang, Ecke & Shishkina 2021). Most of these numerical simulations adopt $Pr = 1$, which corresponds to a special parameter space as we shall show in this study.

Previous studies on the Pr effects in Rayleigh–Bénard convection have shown different scaling behaviours depending on Pr . Verzicco & Camussi (1999) investigated Nu as a function of Pr within the interval of [0.0022, 15] using direct numerical simulations and found that $Nu \sim Pr^{0.14}$ for $Pr \leq 0.35$, whereas Nu is almost independent of Pr for $Pr > 0.35$. Other studies in different Pr intervals have shown similar behaviours (e.g. Kerr & Herring 2000; Silano, Sreenivasan & Verzicco 2010; Li *et al.* 2021). In RRBC, Zhong *et al.* (2009) found the heat transfer behaviour for small $Pr \leq 0.7$ differs from moderate Pr . King & Aurnou (2013) also found that the transition from rotating to non-rotating convection of liquid metal substantially differs from that of water. More recently, Abbate & Aurnou (2023) carried out a suite of RRBC experiments in moderate to high Pr fluids, which showed that the bulk interior flows can be described by the CIA force balance, but the heat transfer is controlled by the boundary layers, similar behaviours were also found in plane layers (Oliver *et al.* 2023). The effects of Pr in spherical rotating convection have been considered experimentally (Aubert *et al.* 2001) and numerically (Tilgner & Busse 1997; Christensen 2002; Gillet & Jones 2006). They found that small $Pr < 1$ tends to reduce the heat transfer and promote zonal flows. In particular, Gillet & Jones (2006) noticed that the diffusion-free scaling does not represent the Pr dependence. These studies

pointed out that the value of Pr plays an important role in spherical rotating convection not only in the ON regime but also in the highly supercritical regime.

In this study we build more than 200 numerical models over a wide range of Pr ($10^{-2} \leq Pr \leq 10^2$) to investigate the influence of Pr on the rotating convection in a spherical shell. We show that the diffusion-free scaling for the heat transfer roughly fits the numerical results with $Pr \leq 1$ but has problems to reconcile numerical models with $Pr > 1$ in the geostrophic turbulence (GT) regime. On the other hand, the convective flow speeds with different Pr in the GT regime roughly follow a unified scaling. We also show that the transition behaviours from rotating to non-rotating convection depend on Pr (King & Aurnou 2013). We find that the transition criteria based on heat transfer and flow morphology are different for cases with $Pr > 1$, in which the heat transfer starts to deviate from the rotating scaling as increasing Ra , but the flow structures remain geostrophic. These findings are in line with recent laboratory experiments at moderate to high Pr , which suggested that the interior flows are controlled by the force balance in the bulk but the heat transfer is controlled by the boundary layers (Abbate & Aurnou 2023). On the other hand, our numerical models at low Pr suggest that both heat transfer and convective flow speeds are controlled by the dynamics in the bulk.

2. Numerical models

2.1. Governing equations

We consider Boussinesq convection of homogeneous fluid in a spherical shell of inner radius r_i and outer radius r_o that uniformly rotates at $\boldsymbol{\Omega} = \Omega \hat{\mathbf{z}}$. Convection is driven by a fixed temperature difference $\Delta T = T_i - T_o$ between the inner and outer boundaries, under the gravity $\mathbf{g} = -g_o \mathbf{r}/r_o$. Using the shell thickness $D = r_o - r_i$ as the length scale, Ω^{-1} as the time scale, ΔT as the temperature scale and gravity at the outer boundary g_o as the reference value, the dimensionless governing equations can be expressed as

$$\frac{\partial \mathbf{u}}{\partial t} + \mathbf{u} \cdot \nabla \mathbf{u} + 2\hat{\mathbf{z}} \times \mathbf{u} = -\nabla P + E \nabla^2 \mathbf{u} + \frac{RaE^2}{Pr} T \mathbf{r}, \quad (2.1)$$

$$\frac{\partial T}{\partial t} + \mathbf{u} \cdot \nabla T = \frac{E}{Pr} \nabla^2 T, \quad (2.2)$$

$$\nabla \cdot \mathbf{u} = 0, \quad (2.3)$$

where \mathbf{u} is the velocity, P is the reduced pressure and T is the temperature. The system is defined by three dimensionless control parameters, the Ekman number E , the Rayleigh number Ra and the Prandtl number Pr :

$$E = \frac{\nu}{\Omega D^2}, \quad Ra = \frac{\alpha g_o \Delta T D^3}{\nu \kappa}, \quad Pr = \frac{\nu}{\kappa}. \quad (2.4a-c)$$

Here ν is the kinematic viscosity, κ is the thermal diffusivity and α is the thermal expansion coefficient. The rotational modified Rayleigh number Ra^* is often used in the rotating convection and Ra^* is also the squared convective Rossby number, which is used in many rotating convection studies (e.g. Gilman 1977; Gastine *et al.* 2013). We have

$$Ra^* = \frac{\alpha_T g_o \Delta T}{\Omega^2 D} = \frac{RaE^2}{Pr} = Ro_c^2, \quad (2.5)$$

which provides a clear relationship between thermal buoyancy and the Coriolis force in rotating convection.

Scaling behaviour of rotating convection

In this study we fix the radius ratio of the shell $\eta = r_i/r_o = 0.35$. Both boundaries are impermeable, no-slip and held at constant temperatures.

2.2. Numerical technique

We use the open-source code XSHELLS (<https://www.bitbucket.org/nschaeff/xshells/>) to solve the governing equations (2.1)–(2.3) subjected to the boundary conditions. The fluid is assumed to be incompressible, and the velocity \mathbf{u} can be decomposed into toroidal and poloidal components:

$$\mathbf{u} = \nabla \times (\mathcal{T}\mathbf{r}) + \nabla \times \nabla \times (\mathcal{P}\mathbf{r}). \quad (2.6)$$

The toroidal \mathcal{T} and poloidal \mathcal{P} scalar fields and the temperature field T are expanded in terms of spherical harmonic expansion on spherical surfaces. The code XSHELLS uses a second-order finite differences method in the radial direction and pseudo-spectral spherical harmonic expansion. The spectral expansion is truncated up to spherical harmonics of degree L_{max} and Nr denotes the number of radial grid points. The time-stepping scheme is second order, and treats the diffusive terms implicitly, while the nonlinear and Coriolis terms are handled explicitly. This code also uses the SHTns library to speed up the spherical harmonic transformations (Schaeffer 2013).

2.3. Diagnostics

We analyse several diagnostics properties to quantify the influence of different control parameters on heat and momentum transports. We adopt several notations regarding averaging procedures. Overbars $\overline{\cdot\cdot\cdot}$ correspond to temporal averaging, angular brackets $\langle \cdot\cdot\cdot \rangle$ to spatial averaging over the entire spherical shell volume and $\langle \cdot\cdot\cdot \rangle_s$ to an average over a spherical surface:

$$\bar{f} = \frac{1}{\tau} \int_{t_0}^{t_0+\tau} f \, dt, \quad \langle f \rangle = \frac{1}{V} \int_V f(r, \theta, \phi) \, dV, \quad \langle f \rangle_s = \frac{1}{4\pi} \int_0^{2\pi} \int_0^\pi f(r, \theta, \phi) \sin \theta \, d\theta \, d\phi, \quad (2.7a-c)$$

where τ is the time averaging interval, V is the volume of the spherical shell, r is the radius, θ is the colatitude and ϕ is the longitude.

The Nusselt number Nu denotes heat transport, the ratio of the total heat flux to the conduction heat flux. In spherical shells the conductive temperature profile T_c is the solution of

$$\frac{dT_c}{dr} = -\frac{r_i r_o}{r^2}, \quad T_c(r_i) = 1, \quad T_c(r_o) = 0. \quad (2.8a-c)$$

Following Gastine, Wicht & Aurnou (2015) yields

$$T_c(r) = \frac{\eta}{(1-\eta)^2} \frac{1}{r} - \frac{\eta}{1-\eta}, \quad (2.9)$$

where $\eta = r_i/r_o$ is the radius ratio. The notation ϑ is introduced to define the time and horizontally averaged radial dimensionless temperature profile

$$\vartheta(r) = \overline{\langle T \rangle_s}. \quad (2.10)$$

Then the Nusselt number is

$$Nu = -\eta \frac{d\vartheta}{dr}(r = r_i) = -\frac{1}{\eta} \frac{d\vartheta}{dr}(r = r_o). \quad (2.11)$$

Here we only consider the global averaged Nu , but the efficiency of convective heat transfer slightly varies as latitude in rotating convection (Wang *et al.* 2021; Gastine & Aurnou 2023). The total kinetic energy is given by

$$E_k = \frac{1}{2} \int_v u^2 dV = \sum_{l=1}^{l_{max}} \sum_{m=0}^l \mathcal{E}_l^m(t), \quad (2.12)$$

where \mathcal{E}_l^m is the dimensionless kinetic energy at a spherical harmonic degree l and order m . The total kinetic energy can be decomposed into zonal and non-zonal parts:

$$E_{zon} = \frac{1}{2} \int_v (u_\phi^0)^2 dV, \quad E_{non} = E_k - E_{zon}. \quad (2.13a,b)$$

We define the Rossby number as

$$Ro = \frac{U_{rms}}{\Omega D}, \quad (2.14)$$

where U_{rms} is the dimensional root-mean-square velocity. Based on the non-dimensionalisation we used, the Rossby number can be determined through kinetic energy as

$$Ro = \sqrt{\frac{2E_k}{V}}. \quad (2.15)$$

Accordingly, we have the non-zonal Rossby number

$$Ro_{non} = \sqrt{\frac{2E_{non}}{V}}, \quad (2.16)$$

and the zonal Rossby number is

$$Ro_{zon} = \sqrt{\frac{2E_{zon}}{V}}. \quad (2.17)$$

We also define the local Rossby number Ro_ℓ as

$$Ro_\ell = \frac{U_{rms}}{\Omega \ell} = Ro \frac{D}{\ell}, \quad (2.18)$$

where ℓ is the typical flow length scale and is determined from the time-averaged kinetic energy spectrum following Christensen & Aubert (2006),

$$\ell^{-1} = \left(\frac{D \sum_{l=1}^{l_{max}} \sum_{m=0}^l l \mathcal{E}_l^m(t)}{\pi \sum_{l=1}^{l_{max}} \sum_{m=0}^l \mathcal{E}_l^m(t)} \right). \quad (2.19)$$

In rotating spherical shell convection the zonal flow component does not contribute to the heat transport from the inner to the outer shell, so we focus on the non-zonal component and it can be determined through the non-zonal Rossby number as

$$Re_{non} = \frac{Ro_{non}}{E}, \quad (2.20)$$

and the zonal Reynolds number is

$$Re_{zon} = \frac{Ro_{zon}}{E}. \quad (2.21)$$

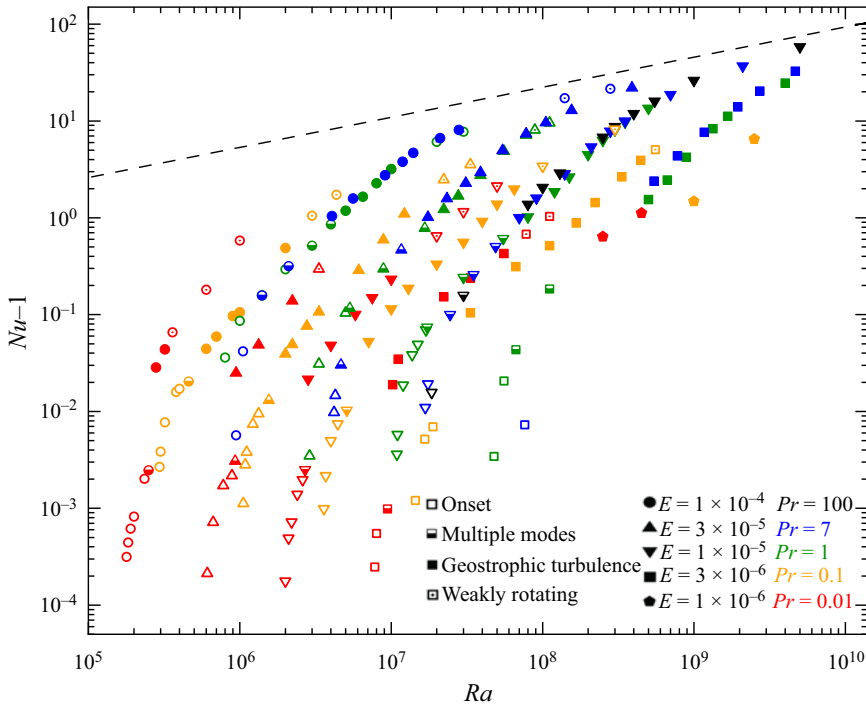


Figure 1. Regime diagram of all numerical models in the parameter space $(Nu - 1, Ra)$. Different colours and shapes correspond to different Pr and E . Open symbols denote the onset (ON) regime; half-filled symbols denote the multiple modes (MM) regime; filled symbols denote the geostrophic turbulence (GT) regime; central dot symbols denote the weakly rotating (WR) regime. The dashed line corresponds to the non-rotating scaling $(Nu - 1) \propto Ra^{1/3}$.

3. Numerical results

3.1. Overview

We have simulated a total of 211 cases in the parameter space of $1.79 \times 10^5 \leq Ra \leq 5 \times 10^9$, $1 \times 10^{-6} \leq E \leq 1 \times 10^{-4}$ and $0.01 \leq Pr \leq 100$. Details of input and diagnostic parameters for all models are listed in table 1 in Appendix A. Figure 1 shows $Nu - 1$ as a function of Ra for all the numerical models. We use different colours and shapes to distinguish different values of Pr and E , respectively. Broadly speaking, the $(Nu - 1, Ra)$ diagram shows that Nu is insensitive to Pr when $Pr \geq 1$ (black, blue and green symbols) but highly dependent on Pr when $Pr < 1$ (orange and red symbols). This is in line with previous studies on the Pr effects in Rayleigh–Bénard convection (Verzicco & Camussi 1999), and suggests that we need to consider different scaling behaviours for small Pr and large Pr .

We also see from figure 1 that slopes of $Nu - 1$ change as Ra increases because of different convective regimes. Our numerical models can be separated into four different regimes depending on the flow morphology and heat transport efficiency. When the Rayleigh number is slightly above the critical value Ra_c , convection is characterised by a single ON mode, which is referred to as the ON regime (open symbols in figure 1). The critical Ra_c and the structure of the ON mode depend on E and Pr (see table 2 in Appendix B). In the ON regime, weak convection has little contribution to the heat transfer, so we can see that $(Nu - 1) \ll 1$ but increases steeply as a function of Ra . As we increase

Ra , the convective flow remains laminar, but several convective modes can coexist, which is referred to as the multiple modes (MM) regime (half-filled symbols in figure 1). In the MM regime the Nusselt number remains small, i.e. $(Nu - 1) < 1$, meaning that heat is mainly transferred by conduction. Further increasing Ra , convection becomes more complex and even turbulent but exhibits columnar structures along the rotation axis, which is referred to as the GT regime (filled symbols in figure 1). As the transition from laminar to turbulent flow is not always well defined, it is not straightforward to define the boundary between the MM and GT regimes. There exists sudden jumps of $Nu - 1$ as increasing Ra for $Pr < 1$ cases (see red and orange symbols in figure 1), so we define such jumps as the boundary between the MM and GT regimes when $Pr < 1$. However, $Nu - 1$ smoothly increases as Ra increases when $Pr \geq 1$, so we simply define $Nu > 2$ as the criterion to enter the GT regime for $Pr \geq 1$ cases following Gastine *et al.* (2016). This criterion amounts to saying that the heat transported by convection overtakes the conductive heat transfer. When Ra is sufficiently large for fixed E and Pr , convection becomes less geostrophic by breaking the rotational constraint and eventually approaches non-rotating convection. Again it is not straightforward to define the transition from rotating to non-rotating turbulence. Some scalings and criteria have been proposed to characterise the transition from rotating to non-rotating convection (Julien *et al.* 2012; Gastine *et al.* 2016; Long *et al.* 2020), but it is difficult to reconcile numerical simulations with different Pr as we shall show. Here we simply use the local Rossby number $Ro_\ell > 0.1$ as the criterion for the weakly rotating (WR) regime (central dot symbols in figure 1). The local Rossby number is the ratio of advection to Coriolis force and $Ro_\ell \lesssim 0.1$ is often seen as an indicator of rotating flows (e.g. Davidson 2014). This criterion is a bit subjective but we do see that the columnar structures tend to break when $Ro_\ell > 0.1$. We define different flow regimes to facilitate our following discussions, but determining the regime boundaries is not the focus of this study.

Figures 2 and 3 show typical flow structures of four different regimes for cases with $Pr = 7$ and $Pr = 0.01$, respectively. We have mentioned that the heat transfer exhibits different behaviours between models with $Pr \geq 1$ and $Pr < 1$. Such differences are also reflected in the flow structures in all regimes. In the ON regime the convective mode at $Pr = 7$ takes the form of columnar rolls in the vicinity of the tangent cylinder (Dormy *et al.* 2004; Barik *et al.* 2023), while the convection at $Pr = 0.01$ shows spiralling columnar structures that occur in the whole domain outside the tangent cylinder (Zhang 1992). The spiralling structure corresponds to the transitional onset between the viscous convection and inertial convection (Zhang & Liao 2017). In the MM regime the convective flows are similar to the ON modes but apparently show other unstable modes coexisting. We will show in §3.3 that the interaction of MM may take place in triadic resonances (Lin 2021). In the GT regime, convection flows are chaotic in the equatorial plane but are organized along the rotation axis. The horizontal length scale is dramatically different between cases with $Pr = 7$ and $Pr = 0.01$ in the same E . In the case of $E = 1 \times 10^{-5}$ and $Pr = 7$, the range of ℓ is 0.064–0.089. However, when $Pr = 0.01$, the range of ℓ is 0.488–0.529. In the WR regime, columnar convective structures are broken as the rotational constraint becomes less important. Figures 2 and 3 provide an overview of the flow morphology in different regimes. In the following we focus on the scaling behaviours of the heat transfer and typical convective flow speeds in terms of control parameters Ra , E and Pr .

3.2. Onset regime

We have shown the flow structures of convection ON modes are different depending on Pr . In this subsection we show scaling behaviours of the heat transfer and

Scaling behaviour of rotating convection

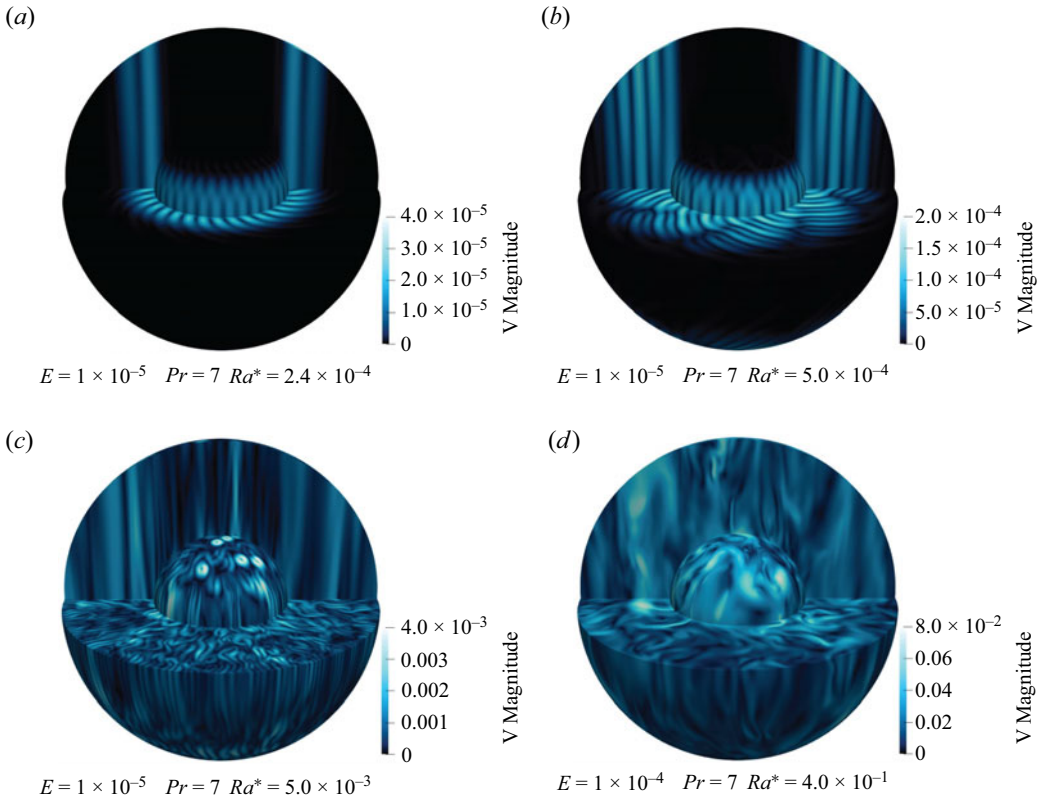


Figure 2. Contours of velocity magnitude in units of the Rossby number at meridional and equatorial planes, and spherical surfaces showing typical flow structures of four different regimes with $Pr = 7$. The inner (outer) surface corresponds to a spherical surface of radius $r_i + 0.1D$ ($r_o - 0.1D$). The colour bar represents Rossby number Ro . (a) The ON regime; (b) MM regime; (c) GT regime; (d) WR regime.

convective flow speed near the onset, with particular attention to Pr dependence. The critical Rayleigh number Ra_c and azimuthal wavenumber m_c of the ON mode are given in table 2 for different E and Pr . It has been shown that the convective heat transport increases linearly with Ra/Ra_c near the onset (Busse & Or 1986; Gillet & Jones 2006),

$$(Nu - 1) \propto \left(\frac{Ra}{Ra_c} - 1 \right). \quad (3.1)$$

Figure 4(a) shows $Nu - 1$ as a function of $Ra/Ra_c - 1$ for the cases in the ON regime. We see that $Nu - 1$ is linearly proportional to $Ra/Ra_c - 1$ as predicted, but the prefactor of the scaling (3.1) depends on Pr , which reflects the Pr dependence of the convection onset. For numerical models with $Pr \geq 1$, the prefactor is similar for different Pr but weakly depends on E , corresponding to the viscous convection mode. At low $Pr < 1$, the ON modes become spiralling columnar structures that fill the whole domain outside the tangent cylinder (figure 3a), corresponding to the transitional mode between viscous convection and inertial convection (Zhang 1992). As the ON mode and critical Ra_c depends on Pr in the transitional convection, the prefactor in the scaling (3.1) also highly

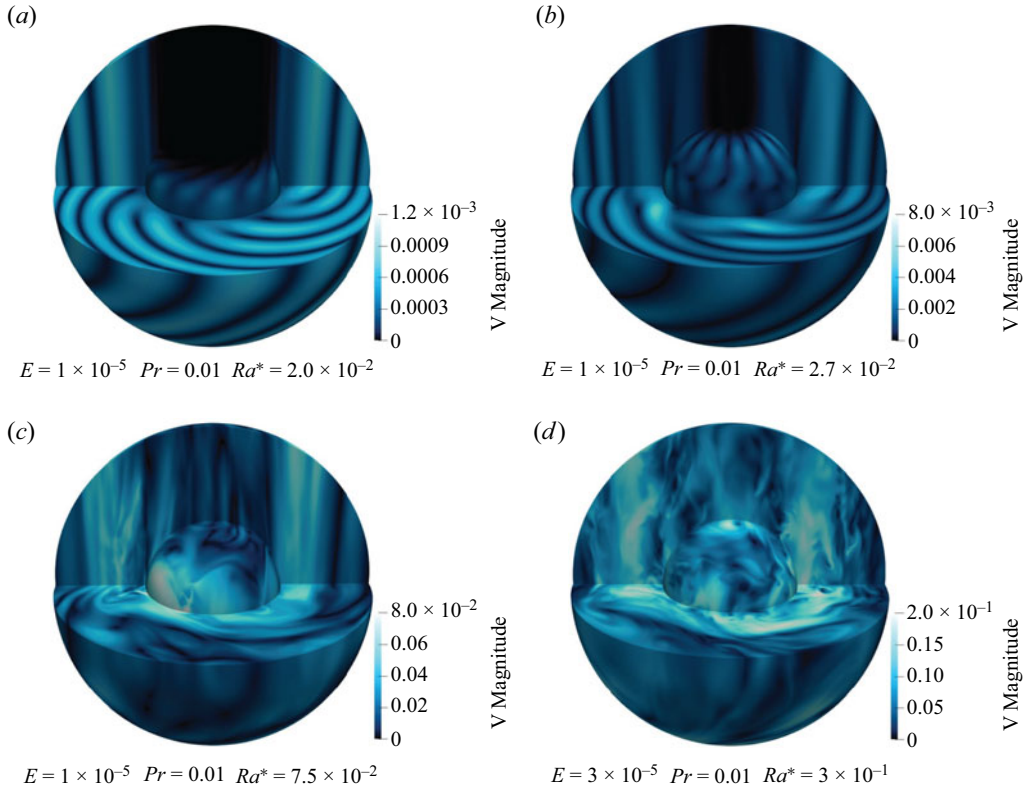


Figure 3. Same as figure 2 but for cases with $Pr = 0.01$. (a) The ON regime; (b) MM regime; (c) GT regime; (d) WR regime.

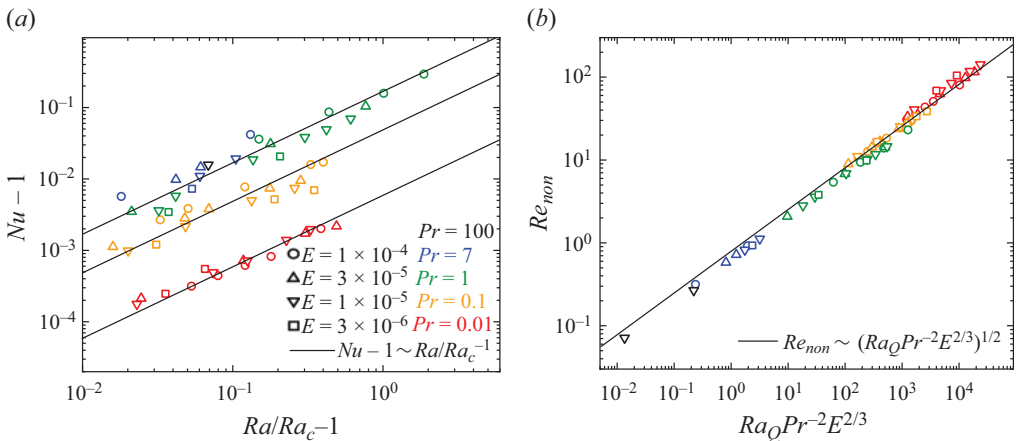


Figure 4. (a) Nusselt number $Nu - 1$ as a function of $Ra/Ra_c - 1$ in the ON regime; (b) Re_{non} as a function of $Ra_Q Pr^{-2} E^{2/3}$ in the ON regime. Different colours and shapes represent different values of Pr and E .

depends on Pr when $Pr < 1$. Our numerical models do not reach sufficiently low Pr to show the purely inertial convection in which the onset of convection is in the form of inertial modes (Zhang 1994).

Scaling behaviour of rotating convection

For the convective flow speed Re_{non} near the onset, a scaling based on the visco-Archimedean–Coriolis (VAC) force balance has been proposed (Aubert *et al.* 2001; King & Buffett 2013; King, Stellmach & Buffett 2013):

$$Re_{non} \sim Ra_Q^{1/2} Pr^{-1} E^{1/3}. \quad (3.2)$$

Here $Ra_Q = (Nu - 1)Ra$ is the flux-based Rayleigh number. The above VAC scaling can also be derived from the balance between the viscous dissipation rate and work done by the buoyancy force (Gastine *et al.* 2016). Figure 4(b) shows Re_{non} vs $Ra_Q Pr^{-2} E^{2/3}$ for all cases near the onset. We can see that numerical results with different Pr fit well a unified VAC scaling (3.2). We note that the VAC scaling is given in terms of Ra_Q that implicitly carries the Pr dependence of Nu . The VAC scaling has been confirmed by previous numerical simulations at Pr around unity (Gastine *et al.* 2016; Long *et al.* 2020). At low Pr in our numerical model, convection near the onset presumably should be the transitional convection (Zhang 1992), in which the effect of inertial force is gradually becoming apparent. However, the VAC scaling tends to be still valid for our numerical models at low Pr . This means that the Pr we calculated is still not small enough to reach the inertial ON regime where the inertial force plays a dominant role.

In summary for the ON regime, both the heat transfer and typical convective flow speed can be explained by previous theoretical predictions. The prefactor of the heat transfer scaling depends on Pr , which reflects the Pr dependence of the convection ON mode.

3.3. Multiple modes regime

As we increase Ra , the convective flow remains laminar but exhibits several mode interactions (figures 2b and 3b). We refer to such flow patterns as the MM regime, which corresponds to a transition from simple convection ON modes to more complex convection modes. As this regime exists only in a narrow parameter range (see figure 1), we do not analyse systematic scaling behaviours but focus on the characteristics of MM interaction in the MM regime.

Previous numerical simulations (Horn & Schmid 2017; Lam, Kong & Zhang 2018) and laboratory experiments (Aurnou *et al.* 2018) using liquid gallium ($Pr \approx 0.025$) observed multiple mode interactions in rotating convection. More recently, Lin (2021) revealed that the MM interaction take place in the form of triadic resonances in spherical rotating convection at low $Pr \leq 0.01$. Triadic resonance is a generic instability mechanism in rotating fluids (Kerswell 2002; Le Bars, Cébron & Le Gal 2015), in which a primary inertial mode with azimuthal wavenumber m_0 and frequency ω_0 can excite a pair of unstable inertial modes with wavenumbers m_1, m_2 and frequencies ω_1, ω_2 matching the resonance conditions:

$$\omega_0 = \omega_1 \pm \omega_2, \quad m_0 = m_1 \pm m_2. \quad (3.3a,b)$$

In this study we find that triadic resonances can take place at both small and moderate Pr . Figure 5 shows time-averaged energy spectra (a,c) and time evolution of the kinetic energy contained in the four dominant components (b,d) for two cases with $Pr = 0.1$ (a,b) and $Pr = 7$ (c,d). For the case with $Pr = 0.1$, the four highest peaks in the m spectrum correspond to $m = 11, 0, 9, 2$, respectively. The $m = 11$ component represents the primary convective mode, while the $m = 0$ component can be attributed to the mean flow generated by the nonlinear interaction of the primary mode (Zhang & Liao 2017). As the energy in the primary mode saturated, two other components with $m = 2$ and $m = 9$ that satisfy the triadic resonance condition start to exponentially grow and then saturate. This is a typical

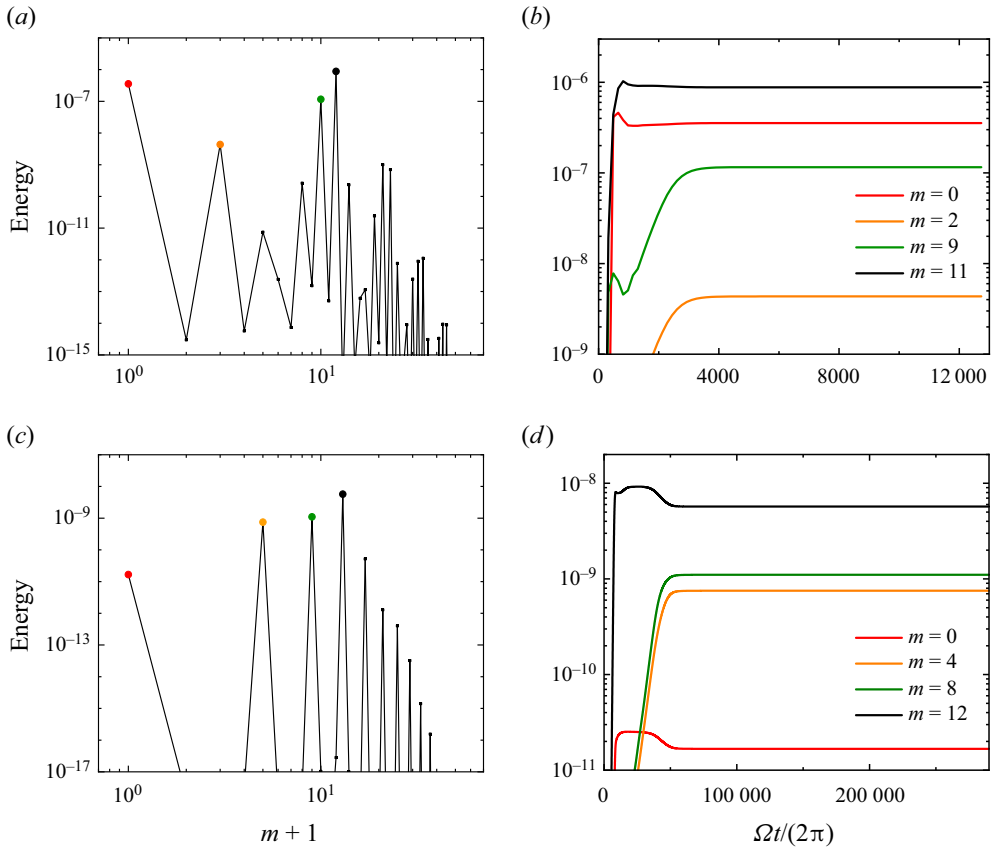


Figure 5. Energy spectra of two cases in the MM regime with possible triadic resonances. (a,b) The case with $E = 1 \times 10^{-5}$, $Pr = 0.1$ and $Ra = 5.1 \times 10^6$; (c,d) the case with $E = 3 \times 10^{-5}$, $Pr = 7$ and $Ra = 4.67 \times 10^6$. (a,c) Time-averaged kinetic energy spectrum as a function of the azimuthal wavenumber m . (b,d) Time evolution of the kinetic energy contained in different m components indicated by circles in the left panel.

behaviour of the triadic resonance (Lin 2021) and suggests that two secondary modes are excited through the triadic resonance with the primary mode. The case with $Pr = 7$ in the bottom panel exhibits similar behaviours but with the primary mode of $m = 12$ and two secondary modes of $m = 4$ and $m = 8$. We should note that triadic resonances at moderate Pr should be due to nonlinear interactions of three thermal Rossby waves rather than purely inertial waves at very low Pr rotating convection (Lin 2021) or in the mechanical driven rotating flows (Le Bars *et al.* 2015).

Our numerical results, in line with the early work of Lin (2021), suggest that the triadic resonance may provide a generic mechanism of the transition from the single ON mode to MM coexisting in rotating convection with both small and moderate Pr . Further increasing Ra would excite more and more unstable modes and eventually lead to turbulent convection that will be discussed in the following subsection.

3.4. Geostrophic turbulence regime

Geostrophic turbulence is thought to be the most relevant regime to convection in rapidly rotating stars and planets. Both the flow morphology and scaling behaviours of heat transfer and momentum transport have been extensively discussed in previous studies

Scaling behaviour of rotating convection

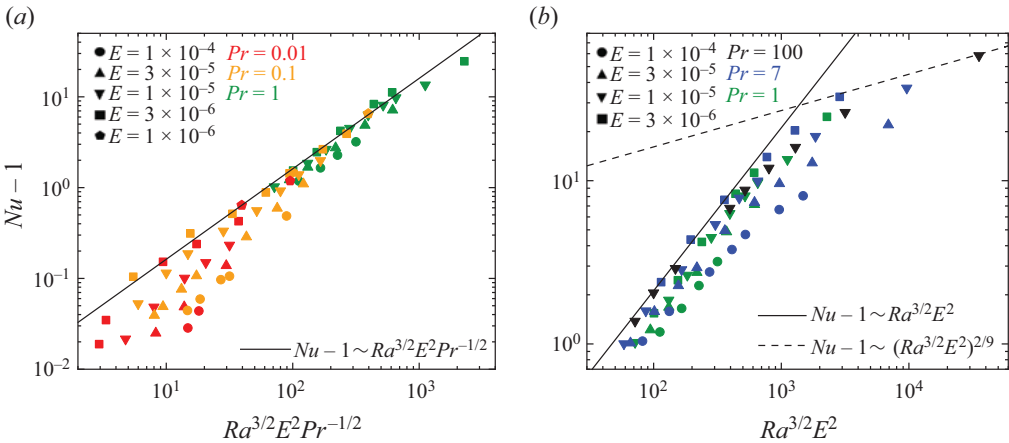


Figure 6. Nusselt number versus control parameters in the GT regime: (a) $Nu - 1$ as a function of $Ra^{3/2}E^2Pr^{-1/2}$ for cases with $Pr \leq 1$, (b) $Nu - 1$ as a function of $Ra^{3/2}E^2$ for cases with $Pr \geq 1$. Different shapes and colours represent different E and Pr as in figure 1.

(e.g. Aurnou *et al.* 2015). In this section we focus on the scaling behaviours of heat transfer Nu and the convective flow speed Re_{non} at different Pr .

In the GT regime the well-known diffusion-free scalings have been widely discussed and compared with numerical simulations and laboratory experiments (Cheng *et al.* 2018; Hawkins *et al.* 2023). The diffusion-free scalings (also called inertial scalings or CIA scalings) were derived using different approaches and arguments in the literature (e.g. Stevenson 1979; Aubert *et al.* 2001; Gillet & Jones 2006; Julien *et al.* 2012; Barker *et al.* 2014; Aurnou *et al.* 2020), which are essentially based on the CIA force balance and the mixing length theory, leading to scalings independent of the fluid viscosity and thermal diffusivity. These scalings predict that the efficiency of convective heat transfer follows

$$(Nu - 1) \sim Ra^{3/2}E^2Pr^{-1/2}, \quad (3.4)$$

and the convective flow speeds follow

$$Re_{non} \sim (Ra_Q Pr^{-2} E^{1/2})^{2/5}, \quad (3.5)$$

where $Ra_Q = (Nu - 1)Ra$ is the flux-based Rayleigh number. Previous studies found that the scalings ((3.4) and (3.5)) can fit numerical and experimental data in a certain parameter regime, but most numerical simulations set Pr around unity and laboratory experiments usually use water ($Pr \approx 7$) as the working fluid (but see other rotating convection experiments with different Pr , e.g. Aurnou *et al.* 2018; Abbate & Aurnou 2023). Systematic tests of the diffusion-free scalings over a wide range of Pr seem to still be lacking. Here we compare the diffusion-free scalings with our numerical models over a wide range of Pr ($10^{-2} \leq Pr \leq 10^2$).

Figure 6 shows $Nu - 1$ as a function of the control parameters Ra , E and Pr in the GT regime. As already noted from figure 1, a single scaling is not able to reconcile numerical results with different Pr because $Nu - 1$ highly depends on Pr when $Pr \leq 1$ and becomes nearly independent of Pr when $Pr \geq 1$. Therefore, in figure 6 we plot $Nu - 1$ separately for cases with $Pr \leq 1$ and $Pr \geq 1$. We can see from figure 6(a) that the diffusion-free scaling (3.4) matches numerical data reasonably well with $Pr \leq 1$ and $(Nu - 1) \geq 1$, except for some data points in the left-bottom corner that correspond to cases with $(Nu - 1) < 1$.

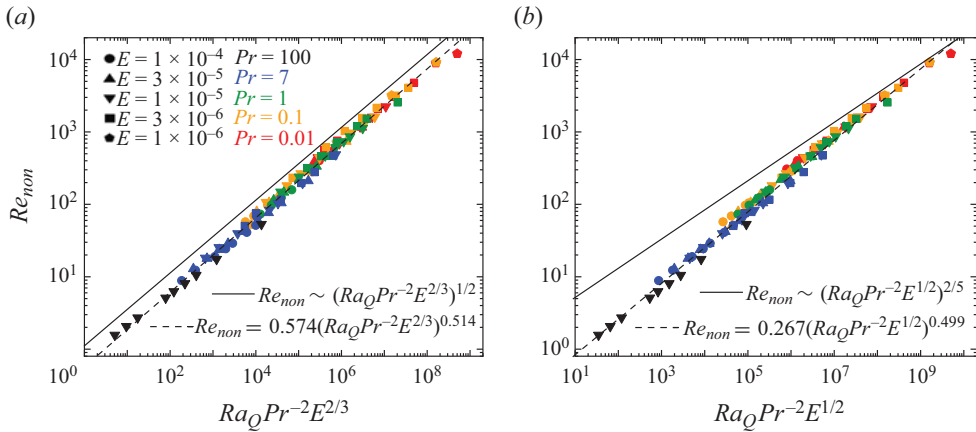


Figure 7. Non-zonal Reynolds number Re_{non} versus control parameters in the GT regime: (a) Re_{non} as a function of $Ra_Q Pr^{-2} E^{2/3}$, where the solid black line corresponds to the VAC scaling (3.2); (b) Re_{non} as a function of $Ra_Q Pr^{-2} E^{1/2}$, where the solid black line corresponds to the CIA scaling (3.5). The dashed lines corresponds to the least-square fit to the data.

In these cases, the convective flow becomes chaotic but Nu remains small because of efficient thermal conduction at small Pr . The diffusion-free scaling is expected to be valid in the asymptotic regime of $Nu \gg 1$. However, it is a huge numerical challenge to achieve large Nu but remain in the GT regime with small Pr , as this would require reducing E and increasing Ra meanwhile. So we find that the diffusion-free scaling (3.4) for the convective heat transfer tends to be valid when $Pr \leq 1$ and $(Nu - 1) \geq 1$ based on our numerically accessible models.

As Nu becomes nearly independent of Pr when $Pr \geq 1$ (in figure 1), figure 6(b) plots $Nu - 1$ as a function of $Ra^{3/2} E^2$ without Pr dependence for cases with $Pr \geq 1$ in the GT regime. Here we basically drop the Pr dependency and keep the same power law for Ra and E as in the diffusion-free scaling (3.4) for reference. We can see that $Nu - 1$ does not show obvious dependence on Pr for fixed Ra and E . The almost independence of Nu on Pr at moderate and large Pr is in line with previous studies on non-rotating convection (Verzicco & Camussi 1999; Li *et al.* 2021). The scattering of data points from the solid line in figure 6(b) is mainly due to different Ekman numbers (different shapes in the plot), suggesting that the power law E^2 is also not suitable for the E dependence. For fixed E and Pr , we see that $Nu - 1$ is proportional to $Ra^{3/2}$ mostly but tends to deviate from the power law $Ra^{3/2}$ and approaches the non-rotating power law $Ra^{1/3}$ at large Ra , although the convection remains rotationally dominated based on the criterion of $Ro_\ell < 0.1$. We discuss the transition from rotating turbulent convection to non-rotating convection in § 3.5. In short, figure 6(b) shows that the widely used diffusion-free scaling (3.4) for the convective heat transfer does not fit our numerical models with $Pr \geq 1$ in the GT regime, which is also shown by recent laboratory experiments with moderate to high Pr (Abbate & Aurnou 2023).

We now turn to examine the scaling behaviour of the convective flow speed measured by the non-zonal Reynolds number Re_{non} . Figures 7(a) and 7(b) show comparisons of Re_{non} from numerical models in the GT regime with the VAC scaling and the CIA scaling, respectively. By comparing the results of least-squares fitting, we find that our numerical results more closely collapse on the VAC scaling. However, we note that the flow speed tends to approach the CIA scaling at low Pr and large Re_{non} ($\gtrsim 10^3$). This implies that the

viscosity plays a non-negligible role in most of our numerical models. It is interesting that convective velocities roughly follow a unified scaling, despite the very different scaling behaviours for the heat transfer. However, we should mention that both the VAC and CIA scalings are given in terms of the flux-based Rayleigh number $Ra_Q = (Nu - 1)Ra$, which already takes into account different scaling behaviours of $Nu - 1$. The scaling behaviour of the convective velocities in our numerical simulations is also in agreement with recent RRBC laboratory experiments at different Pr (Abbate & Aurnou 2023).

In summary for the GT regime, both heat transfer and convective velocities asymptotically approach the diffusion-free scalings at low $Pr \leq 1$, suggesting that both the global heat transfer and convective flows are controlled by inviscid dynamics in the bulk. At large $Pr > 1$, the efficiency of heat transfer becomes nearly independent of Pr and approaches the non-rotating scaling at large Ra , while the convective velocities closely follow the scaling based on the VAC force balance. The scaling behaviours at large Pr , in line with experimental results of Abbate & Aurnou (2023), suggest that the heat transfer is controlled by the boundary layers, whereas the typical flow speeds are controlled by the interior force balance in currently accessible numerical models.

3.5. Weakly rotating regime

Further increasing Ra , the convective flows become less geostrophic due to the weakening rotational constraint (figures 2d and 3d). At sufficiently large Ra , a strong buoyancy force would break rotational constraints and lead to non-rotating convection. However, the transition from rotating to non-rotating convection does not mean an abrupt regime change. It is not straightforward to quantitatively define when the convection is rotationally dominated. The regime changes from rotating to non-rotating convection have been extensively discussed and several transition criteria were proposed and tested (e.g. King *et al.* 2009; Julien *et al.* 2012; Gastine *et al.* 2016; Long *et al.* 2020), yet no consensus has been reached. As introduced in § 3.1, we use the local Rossby number $Ro_\ell \leq 0.1$ as a tentative criterion for the rotation-dominated convection and, thus, set cases with $Ro_\ell > 0.1$ as the WR regime. In this section we examine changes of the Nusselt number and local Rossby number as increasing Ra from GT to WR regimes. As we shall show the transitional behaviours are rather complicated and it is impractical to define a single transition criteria that can reconcile both the heat transfer and flow morphology with different Pr .

In order to monitor the behaviour changes of the heat transfer, we define a rescaled Nusselt number \tilde{Nu} , i.e.

$$\tilde{Nu} = \begin{cases} \frac{Nu - 1}{Ra^{3/2}E^2} & \text{when } Pr \geq 1, \\ \frac{Nu - 1}{Ra^{3/2}E^2Pr^{-1/2}} & \text{when } Pr \leq 1, \end{cases} \quad (3.6)$$

which takes into account different scalings of $Nu - 1$ at different Pr in the GT regime as shown in figure 6. The rescaled \tilde{Nu} should be flat in the rotation-dominated convection and would start to drop as Ra increases to the WR regime. The turning point is usually seen as a sign for the transition from rotation to non-rotating convection (Long *et al.* 2020).

Figures 8(a) and 8(b) show the rescaled Nusselt number \tilde{Nu} and the local Rossby number Ro_ℓ as a function of $RaE^{8/5}$, which was proposed to be a key control parameter for the transition (Julien *et al.* 2012). We can see that the heat transfer behaviours indeed change at around $RaE^{8/5} \approx 5$ for data points with $Pr \geq 1$, but this criteria does not reconcile data

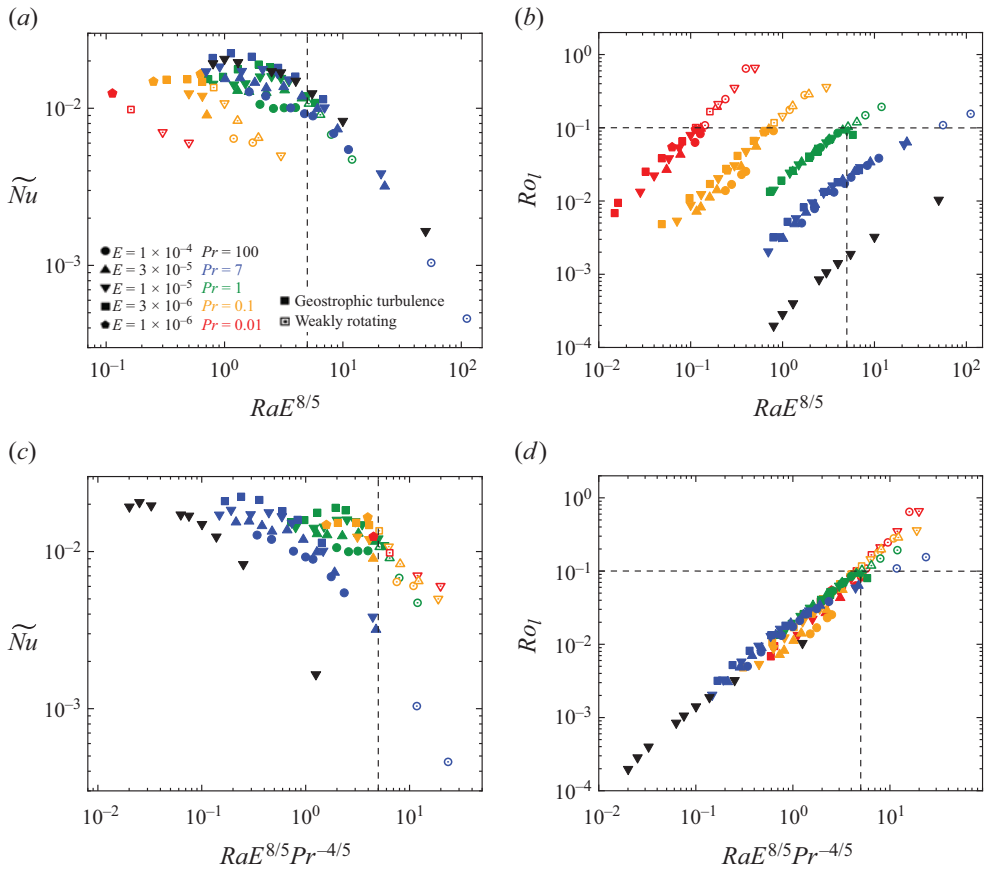


Figure 8. Rescaled Nusselt number \tilde{Nu} and local Rossby number Ro_ℓ in the GT and WR regimes: (a) \tilde{Nu} and (b) Ro_ℓ as a function of $RaE^{8/5}$; (c) \tilde{Nu} and (d) Ro_ℓ as a function of $RaE^{8/5} Pr^{-4/5}$. Data points with $Nu < 2$ are excluded in (a) and (c). Symbols have the same definitions as those in figure 1.

points with low Pr . It is interesting that $RaE^{8/5} \approx 5$ also corresponds to $Ro_\ell \approx 0.1$ at $Pr = 1$. However, the Ro_ℓ at high Pr (blue and black symbols in figure 8b) is still much smaller than 0.1 even when $RaE^{8/5} > 5$. This means that the convective flow remains quite geostrophic in the bulk but the heat transfer already approaches the non-rotating scaling at high Pr . Therefore, the transitional criterion based on the heat transfer and based on the flow morphology would be quite different. This again points to the scenario that the heat transfer is controlled by the boundary layers but the convective flows are controlled by the force balance in the bulk.

Figure 8(b) clearly shows that the Ro_ℓ depends on Pr . By an empirical fitting of data, we find that the Pr dependence can be approximated by a power exponent of around 4/5. Therefore, we define a control parameter

$$Ra_G = RaE^{8/5} Pr^{-4/5}, \tag{3.7}$$

and plot Nu and Ro_ℓ as a function of Ra_G in figure 8(c,d). Gastine *et al.* (2016) derived a similar control parameter of $RaE^{8/5} Pr^{-3/5}$ based on the convective Rossby number Ro_c in the boundary layers. Here we find that $Ra_G = RaE^{8/5} Pr^{-4/5}$ can better fit our numerical data of the Ro_ℓ . Figure 8(d) shows that $Ra_G \approx 5$ corresponds to $Ro_\ell = 0.1$ for all different Pr . We also see from figure 8(c) that $Ra_G \approx 5$ corresponds to the turning point of the

rescaled Nusselt number \widetilde{Nu} for data points with $Pr \leq 1$. This implies that the transition criteria can be unified for the heat transfer and flow morphology at low Pr . The control parameter Ra_G is not suitable to describe the transition of the heat transfer for the model with $Pr > 1$ as expected.

Combining the scaling behaviours shown in § 3.4 and the transitional behaviours in this section, we suggest that the heat transfer is controlled by the boundary layers at large Pr and by the interior dynamics at small Pr . We should mention that $Pr = 1$ corresponds to a quite special parameter regime because data points can fit both Pr -dependent and Pr -independent scalings. The convective flow velocities and flow morphology are mainly controlled by the force balance in the interior. If we characterise the transition from GT to WR based on the Ro_ℓ in the bulk, we find that $Ra_G = RaE^{8/5}Pr^{-4/5}$ provides a unified control parameter for the transition with all different Pr based on our numerical data.

3.6. Mean zonal flows

The above analysis has focused on the scaling behaviour of non-zonal flows, which are related to the heat transfer. Mean zonal flows are spontaneously generated in rotating convection systems due to the nonlinear effects (e.g. Christensen 2002; Miyagoshi, Kageyama & Sato 2010). In this section we show the magnitude of zonal flows and scaling behaviours with different Pr in the GT regime where the zonal flow may be significant. Previous studies have shown that zonal flows are more readily developed at low Prandtl numbers $Pr < 1$ (Zhang 1992; Aubert *et al.* 2001). The zonal flow amplitude is measured by the zonal Reynolds number Re_{zon} as defined in § 2.3. Figure 9(a) shows the ratio of Re_{zon}/Re_{non} as a function of Ra with different E and Pr in the GT regime. We can see that the ratio is around or larger than unity for most cases at $Pr < 1$, suggesting strong zonal flows are generated at low Prandtl numbers. In contrast, most of the cases show the ratio $Re_{zon}/Re_{non} < 1$ when $Pr > 1$. These results are in line with previous numerical and experimental studies on zonal flows driven by rotating convection (Aubert *et al.* 2001; Christensen 2002). It is also found that as Ra increases, Re_{zon}/Re_{non} in both $Pr = 1$ and $Pr = 7$ cases shows a significant increase, especially at relatively low Ekman number $E = 3 \times 10^{-6}$. This demonstrates that at sufficiently small E and large Ra , the zonal flows can become dominant over the non-zonal flows even at high Pr . However, within the parameter interval we calculated, dominant zonal flows are more likely to be generated at low Pr .

It is of great interest to see if there is any systematic dependence of the zonal flows on the control parameters. As there is no existing theoretical prediction on scaling of zonal flows in rotating turbulent convection, we made a least-square fitting of Re_{zon} in the form of the power law in control parameters from numerical data with $Re_{zon} \geq 100$. As shown in figure 9(b), the power law scaling $Re_{zon} \sim Ra^{1.29}E^{1.1}Pr^{-1.42}$ (solid black line) can well describe the data. It is found that the zonal flow strength is stronger for $Pr \leq 1$ and, for $Pr \geq 1$, the Re_{zon} hardly exceeds 100 in our simulation interval. The scaling of $Pr^{-1.42}$ demonstrates that the strong zonal flow is more likely to be generated at $Pr \leq 1$ with fixed Ra and E . For $Pr \geq 1$, the strong zonal flow can also be generated by increasing Ra with fixed E .

4. Conclusions and outlooks

In this study we have constructed more than 200 numerical models of rotating convection in a spherical shell over a wide range of Pr from 10^{-2} to 10^2 , which provide a valuable

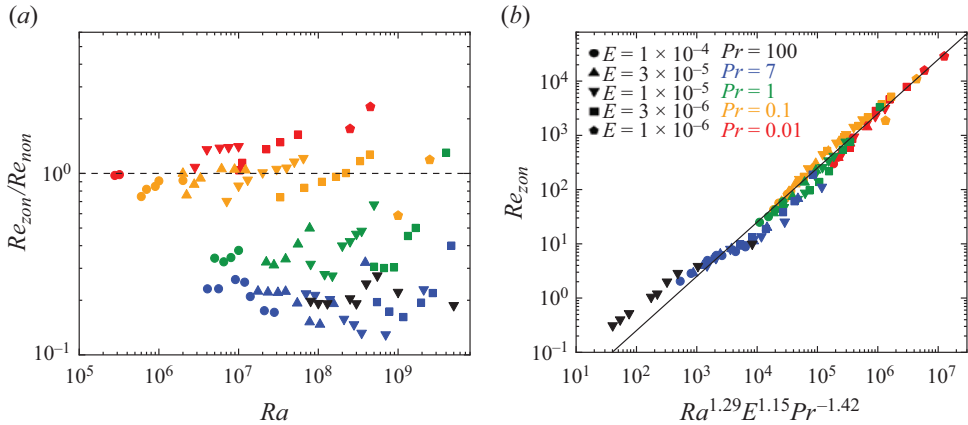


Figure 9. (a) Reynolds number ratio Re_{zon}/Re_{non} as a function of Ra in the GT regime; (b) Re_{zon} as a function of $Ra^{1.29}E^{1.15}Pr^{-1.42}$ in the GT regime. Symbols have the same definitions as those in figure 1.

dataset to investigate the scaling behaviours of rotating convection. Our numerical models are separated into four different flow regimes, namely near the onset, MM interactions, GT and WR regimes. We investigated the scaling behaviours of the heat transfer and convective flow velocities in different flow regimes, with particular attention to the dependence on the Pr .

Near the ON regime, the convective heat transfer is proportional to the supercriticality as predicted but the prefactor depends on the Pr due to different ON modes. The convective velocities can be well described by the VAC scaling. Multiple mode interactions can be seen as a transitional regime from laminar to turbulent convection. In this regime, we show possible evidences of triadic resonances at both low and high Pr , suggesting that the triadic resonance is a generic mechanism for the transition to turbulence in rotating convection.

In the GT regime we find that a single scaling cannot reconcile the heat transfer behaviours of numerical models with different Pr . The heat transfer at low Pr tends to approach the diffusion-free scaling whereas the Nusselt numbers at high Pr become nearly independent of Pr . However, the convective velocities at different Pr roughly follow a unified scaling that is in the VAC force balances, though the scaling tends to approach the CIA force balance at low Pr and large Re_{non} . For the mean zonal flow, we obtain the power law scaling $Re_{zon} \sim Ra^{1.29}E^{1.15}Pr^{-1.42}$ by fitting numerical data in the GT regime.

We also find that the transition behaviours from GT to WR regimes are different depending on Pr , as noted in previous experimental studies (King & Aurnou 2013). At high Pr , the heat transfer already approaches the non-rotating scaling while the convective flows remain rotation-dominated based on the local Rossby number in the bulk. At low Pr , transitions of the heat transfer and flow morphology take place simultaneously, both of which can be roughly determined by the control parameter $Ra_G = RaE^{8/5}Pr^{-4/5}$ according to the empirical fitting of numerical data. In fact, we show that $Ra_G \approx 5$ provides a unified transition criterion for all different Pr if we characterise the transition merely based on the local Rossby number in the bulk.

Both scaling behaviours and transition behaviours suggest that the heat transfer is controlled by the boundary layers whereas the convective flows are controlled by the force balance in the bulk at high Pr (Abbate & Aurnou 2023; Hawkins *et al.* 2023). Both numerical and experimental results show the convective velocities are close to the VAC scaling, suggesting that the viscosity still plays a non-negligible role in currently accessible

numerical simulations and laboratory experiments. At low Pr , it is very difficult to achieve large Nu while maintaining GT to fully test the diffusion-free scalings. In fact, simulations at both low and high Pr pose a huge numerical challenge because of large contrasts of diffusivities. Nevertheless, our numerical models at low Pr show the trend to approach the diffusion-free scalings for both the heat transfer and convective velocities, though it requires further confirmation in more extreme parameter regimes.



Finally, it is of great interest to investigate the effect of Pr on rotating convection in the presence of magnetic fields for planetary core dynamics. Meanwhile, spherical shell rotating convection is latitudinally dependent, as reported by Wang *et al.* (2021), Gastine & Aurnou (2023). In this study we considered only the global averaged scalings that represent the overall dynamics in the system. It would be interesting to explore the scaling of different latitudes under different Pr to complement our study.

Acknowledgements. Numerical simulations made use of the open-source code XSHELLS, which is freely available at <https://nschaeff.bitbucket.io/xshells>. We thank Nathanaël Schaeffer for his assistance in setting up and running the numerical code. The critical Rayleigh numbers and wavenumbers for the onset of convection were calculated using the open-source code MagIC (<https://magic-sph.github.io>). We are very grateful to anonymous reviewers for their constructive comments, which have helped improve the paper.

Funding. This study was supported by the National Key R&D Program of China (grant no. 2022YFF0503200), the National Natural Science Foundation of China (12250012, 42142034, 42350002), the B-type Strategic Priority Program of the CAS (XDB41000000) and the Pearl River Program (2019QN01X189). Numerical calculations were performed on the Taiyi cluster supported by the Center for Computational Science and Engineering of Southern University of Science and Technology.

Declaration of interests. The authors report no conflict of interest.

Author ORCIDs.

-  Wei Fan <https://orcid.org/0000-0001-7612-4024>;
-  Qi Wang <https://orcid.org/0000-0001-6986-3056>;
-  Yufeng Lin <https://orcid.org/0000-0002-7639-9594>.

Appendix A. List of numerical simulations

Table 1 lists all of numerical models presented in this study with detailed control parameters, diagnostic parameters and numerical resolutions. We also created an Excel spreadsheet with more comprehensive data, which is made available on Zenodo (<https://zenodo.org/records/12696528>).

No.	E	Ra^*	$Nu - 1$	Re_{non}	Re_{zon}	ℓ	Regime	$N_r \times L_{max}$
$Pr = 100$								
1	1×10^{-5}	1.85×10^{-5}	0.0157	0.713	—	—	ON	120×120
2	1×10^{-5}	3.0×10^{-5}	0.158	0.267	—	—	MM	140×140
3	1×10^{-5}	8.0×10^{-5}	1.38	1.52	0.311	0.081	GT	180×180
4	1×10^{-5}	1.0×10^{-4}	2.06	2.07	0.399	0.074	GT	200×200
5	1×10^{-5}	1.3×10^{-4}	2.90	2.72	0.522	0.070	GT	220×220
6	1×10^{-5}	2.5×10^{-4}	6.78	5.11	1.04	0.060	GT	240×240
7	1×10^{-5}	3.0×10^{-4}	8.76	6.27	1.20	0.060	GT	260×260

Table 1. For caption see next page.

No.	E	Ra^*	$Nu - 1$	Re_{non}	Re_{zon}	ℓ	Regime	$N_r \times L_{max}$
8	1×10^{-5}	4.0×10^{-4}	11.93	8.09	1.99	0.059	GT	280×280
9	1×10^{-5}	5.5×10^{-4}	16.02	10.53	2.87	0.058	GT	300×300
10	1×10^{-5}	1.0×10^{-3}	26.21	17.45	3.87	0.055	GT	360×360
11	1×10^{-5}	5.0×10^{-3}	58.33	53.16	9.97	0.052	GT	420×420
$Pr = 7$								
12	1×10^{-4}	1.35×10^{-3}	0.0057	0.316	—	—	ON	80×55
13	1×10^{-4}	1.5×10^{-3}	0.0418	0.919	—	—	ON	80×55
14	1×10^{-4}	2.0×10^{-3}	0.158	2.12	—	—	MM	80×55
15	1×10^{-4}	3.0×10^{-3}	0.318	3.27	—	—	MM	80×60
16	1×10^{-4}	5.8×10^{-3}	1.04	8.85	2.05	0.182	GT	100×90
17	1×10^{-4}	8.0×10^{-3}	1.59	12.31	2.85	0.161	GT	120×90
18	1×10^{-4}	1.3×10^{-2}	2.76	19.02	4.95	0.149	GT	120×110
19	1×10^{-4}	1.7×10^{-3}	3.79	24.37	6.13	0.145	GT	120×120
20	1×10^{-4}	2.0×10^{-3}	4.68	29.04	6.09	0.141	GT	120×120
21	1×10^{-4}	3.0×10^{-3}	6.66	41.12	7.20	0.136	GT	150×150
22	1×10^{-4}	4.0×10^{-2}	8.09	51.29	8.80	0.136	GT	180×180
23	1×10^{-4}	2.0×10^{-1}	17.23	158.7	35.06	0.150	WR	260×260
24	1×10^{-4}	4.0×10^{-1}	21.49	245.7	90.04	0.169	WR	320×320
25	3×10^{-5}	5.4×10^{-4}	0.0098	0.58	—	—	ON	96×96
26	3×10^{-5}	5.5×10^{-4}	0.0147	0.72	—	—	ON	96×96
27	3×10^{-5}	6.0×10^{-4}	0.0302	1.08	—	—	MM	96×96
28	3×10^{-5}	1.5×10^{-3}	0.466	6.87	—	—	MM	120×120
29	3×10^{-5}	2.25×10^{-3}	1.01	12.87	2.88	0.129	GT	140×120
30	3×10^{-5}	3.0×10^{-3}	1.58	17.89	3.96	0.113	GT	160×160
31	3×10^{-5}	4.0×10^{-3}	2.28	23.72	5.23	0.104	GT	180×180
32	3×10^{-5}	5.0×10^{-3}	2.93	28.81	6.44	0.099	GT	200×200
33	3×10^{-5}	7.0×10^{-3}	4.95	41.93	8.08	0.096	GT	260×260
34	3×10^{-5}	1.0×10^{-2}	7.36	59.08	8.96	0.092	GT	280×280
35	3×10^{-5}	1.35×10^{-2}	9.60	76.53	11.27	0.092	GT	320×320
36	3×10^{-5}	2.0×10^{-2}	12.86	104.6	20.02	0.094	GT	360×360
37	3×10^{-5}	5.0×10^{-2}	21.99	211.0	68.09	0.105	GT	400×400
38	1×10^{-5}	2.4×10^{-4}	0.011	0.823	—	—	ON	120×100
39	1×10^{-5}	2.5×10^{-4}	0.019	1.12	—	—	ON	120×100
40	1×10^{-5}	3.5×10^{-4}	0.100	3.11	—	—	MM	160×120
41	1×10^{-5}	5.0×10^{-4}	0.259	5.82	—	—	MM	200×160
42	1×10^{-5}	7.0×10^{-4}	0.504	10.16	—	—	MM	200×160
43	1×10^{-5}	1.0×10^{-3}	1.00	18.19	3.96	0.089	GT	200×200
44	1×10^{-5}	1.3×10^{-3}	1.60	25.43	5.42	0.079	GT	200×200
45	1×10^{-5}	2.0×10^{-3}	2.85	39.54	8.00	0.070	GT	240×240
46	1×10^{-5}	3.0×10^{-3}	5.39	61.77	9.73	0.066	GT	320×320
47	1×10^{-5}	4.0×10^{-3}	7.83	83.35	12.24	0.065	GT	320×350
48	1×10^{-5}	5.0×10^{-3}	9.96	103.3	13.64	0.064	GT	400×400
49	1×10^{-5}	1.0×10^{-2}	18.69	196.6	25.42	0.069	GT	420×420
50	1×10^{-5}	3.0×10^{-2}	36.95	487.8	111.7	0.085	GT	480×460
51	3×10^{-6}	9.8×10^{-5}	0.0073	0.933	—	—	ON	160×160
52	3×10^{-6}	7.0×10^{-4}	2.39	50.39	9.85	0.049	GT	250×250
53	3×10^{-6}	1.0×10^{-3}	4.36	75.46	13.08	0.042	GT	320×320
54	3×10^{-6}	1.5×10^{-3}	7.64	116.2	18.77	0.043	GT	360×360
55	3×10^{-6}	2.5×10^{-3}	13.97	197.0	38.23	0.045	GT	400×400

Table 1. For caption see next page.

Scaling behaviour of rotating convection

No.	E	Ra^*	$Nu - 1$	Re_{non}	Re_{zon}	ℓ	Regime	$N_r \times L_{max}$
56	3×10^{-6}	3.5×10^{-3}	20.34	278.2	60.96	0.048	GT	480×480
57	3×10^{-6}	6.0×10^{-3}	32.67	473.0	189.1	0.058	GT	600×560
$Pr = 1$								
58	1×10^{-4}	8.0×10^{-3}	0.036	5.396	—	—	ON	80×50
59	1×10^{-4}	1.0×10^{-2}	0.086	9.374	—	—	ON	100×60
60	1×10^{-4}	1.4×10^{-2}	0.158	13.90	—	—	ON	120×70
61	1×10^{-4}	2.0×10^{-2}	0.294	23.04	—	—	ON	120×70
62	1×10^{-4}	3.0×10^{-2}	0.515	39.10	—	—	MM	120×80
63	1×10^{-4}	4.0×10^{-2}	0.855	57.02	—	—	MM	120×100
64	1×10^{-4}	5.0×10^{-2}	1.18	73.31	25.01	0.196	GT	120×110
65	1×10^{-4}	6.5×10^{-2}	1.65	97.17	31.66	0.190	GT	140×140
66	1×10^{-4}	8.0×10^{-2}	2.28	123.9	42.61	0.194	GT	160×160
67	1×10^{-4}	1.0×10^{-1}	3.19	159.0	59.89	0.201	GT	160×160
68	1×10^{-4}	2.0×10^{-1}	6.08	282.9	138.4	0.212	WR	200×200
69	1×10^{-4}	3.0×10^{-1}	7.76	373.2	213.9	0.223	WR	240×240
70	3×10^{-5}	2.6×10^{-3}	0.0035	2.078	—	—	ON	100×63
71	3×10^{-5}	3.0×10^{-3}	0.0310	6.806	—	—	ON	120×90
72	3×10^{-5}	4.5×10^{-3}	0.104	14.31	—	—	ON	120×100
73	3×10^{-5}	4.8×10^{-3}	0.116	15.49	—	—	MM	120×100
74	3×10^{-5}	8.0×10^{-3}	0.296	34.20	—	—	MM	140×110
75	3×10^{-5}	1.5×10^{-2}	0.788	81.48	—	—	MM	180×150
76	3×10^{-5}	2.0×10^{-2}	1.22	114.2	37.00	0.143	GT	200×180
77	3×10^{-5}	2.5×10^{-2}	1.68	146.6	45.79	0.136	GT	200×200
78	3×10^{-5}	3.5×10^{-2}	2.74	219.5	74.01	0.145	GT	240×200
79	3×10^{-5}	5.0×10^{-2}	4.86	334.5	136.2	0.156	GT	240×220
80	3×10^{-5}	7.0×10^{-2}	7.15	455.1	227.1	0.165	GT	280×260
81	3×10^{-5}	8.0×10^{-2}	8.071	515.4	255.8	0.168	WR	280×260
82	3×10^{-5}	1.0×10^{-1}	9.578	602.5	355.3	0.176	WR	320×320
83	1×10^{-5}	1.09×10^{-3}	0.0036	2.82	—	—	ON	120×100
84	1×10^{-5}	1.1×10^{-3}	0.0058	3.58	—	—	ON	160×100
85	1×10^{-5}	1.2×10^{-3}	0.019	6.88	—	—	ON	160×100
86	1×10^{-5}	1.38×10^{-3}	0.038	10.28	—	—	ON	160×100
87	1×10^{-5}	1.5×10^{-3}	0.049	11.70	—	—	ON	160×100
88	1×10^{-5}	1.7×10^{-3}	0.069	14.59	—	—	ON	160×130
89	1×10^{-5}	1.73×10^{-3}	0.074	15.45	—	—	MM	180×130
90	1×10^{-5}	3.0×10^{-3}	0.242	40.82	—	—	MM	200×150
91	1×10^{-5}	5.5×10^{-3}	0.610	96.06	—	—	MM	280×180
92	1×10^{-5}	8.0×10^{-3}	1.02	148.6	47.05	0.110	GT	280×190
93	1×10^{-5}	1.2×10^{-2}	1.86	239.5	66.55	0.103	GT	320×240
94	1×10^{-5}	1.5×10^{-2}	2.64	318.0	86.78	0.105	GT	320×240
95	1×10^{-5}	2.0×10^{-2}	4.49	470.0	187.7	0.122	GT	320×300
96	1×10^{-5}	2.5×10^{-2}	6.30	609.1	257.0	0.124	GT	320×300
97	1×10^{-5}	3.0×10^{-2}	8.08	738.9	342.2	0.130	GT	320×300
98	1×10^{-5}	3.5×10^{-2}	9.74	862.0	415.0	0.132	GT	320×320
99	1×10^{-5}	5.0×10^{-2}	13.30	1126	757.0	0.148	GT	320×320
100	3×10^{-6}	4.3×10^{-4}	0.00344	3.80	—	—	ON	160×100
101	3×10^{-6}	5.0×10^{-4}	0.0207	9.88	—	—	ON	160×100
102	3×10^{-6}	6.0×10^{-4}	0.0434	15.2	—	—	MM	180×120
103	3×10^{-6}	1.0×10^{-3}	0.184	45.5	—	—	MM	200×200
104	3×10^{-6}	4.5×10^{-3}	1.54	317.0	96.96	0.074	GT	260×260

Table 1. For caption see next page.

No.	E	Ra^*	$Nu - 1$	Re_{non}	Re_{zon}	ℓ	Regime	$N_r \times L_{max}$
105	3×10^{-6}	6.0×10^{-3}	2.46	460.8	138.7	0.076	GT	300×300
106	3×10^{-6}	8.0×10^{-3}	4.22	716.4	217.5	0.086	GT	320×320
107	3×10^{-6}	1.2×10^{-2}	8.32	1203	544.2	0.102	GT	360×360
108	3×10^{-6}	1.5×10^{-2}	11.20	1521	761.9	0.108	GT	400×400
109	3×10^{-6}	3.6×10^{-2}	24.64	2551	3320	0.157	GT	480×480
$Pr = 0.1$								
110	1×10^{-4}	2.95×10^{-2}	0.0027	10.56	—	—	ON	100×50
111	1×10^{-4}	3.0×10^{-2}	0.0039	12.73	—	—	ON	100×50
112	1×10^{-4}	3.2×10^{-2}	0.0077	18.35	—	—	ON	100×55
113	1×10^{-4}	3.8×10^{-2}	0.016	28.44	—	—	ON	100×70
114	1×10^{-4}	4.0×10^{-2}	0.017	30.16	—	—	ON	100×70
115	1×10^{-4}	4.6×10^{-2}	0.020	35.47	—	—	MM	100×70
116	1×10^{-4}	6.0×10^{-2}	0.044	57.47	42.88	0.517	GT	100×80
117	1×10^{-4}	7.0×10^{-2}	0.059	69.24	56.57	0.530	GT	120×80
118	1×10^{-4}	9.0×10^{-2}	0.097	97.27	82.49	0.555	GT	120×100
119	1×10^{-4}	1.0×10^{-1}	0.106	104.5	94.99	0.557	GT	150×100
120	1×10^{-4}	2.0×10^{-1}	0.487	282.2	258.2	0.420	GT	200×140
121	1×10^{-4}	3.0×10^{-1}	1.053	494.9	435.8	0.375	WR	250×180
122	1×10^{-4}	4.35×10^{-1}	1.734	750.9	575.8	0.338	WR	280×200
123	3×10^{-5}	9.5×10^{-3}	0.0011	8.96	—	—	ON	100×70
124	3×10^{-5}	9.8×10^{-2}	0.0028	14.29	—	—	ON	100×70
125	3×10^{-5}	1.0×10^{-2}	0.0038	16.69	—	—	ON	100×80
126	3×10^{-5}	1.1×10^{-2}	0.0074	23.83	—	—	ON	100×80
127	3×10^{-5}	1.2×10^{-2}	0.0095	27.58	—	—	ON	120×80
128	3×10^{-5}	1.4×10^{-2}	0.0130	34.76	—	—	MM	120×100
129	3×10^{-5}	1.8×10^{-2}	0.0393	67.03	50.93	0.350	GT	120×120
130	3×10^{-5}	2.0×10^{-2}	0.049	79.30	60.20	0.364	GT	140×120
131	3×10^{-5}	2.5×10^{-2}	0.076	105.6	91.83	0.375	GT	140×130
132	3×10^{-5}	3.0×10^{-2}	0.107	134.2	126.2	0.391	GT	140×130
133	3×10^{-5}	5.5×10^{-2}	0.287	285.2	301.9	0.422	GT	160×140
134	3×10^{-5}	8.0×10^{-2}	0.593	480.3	505.7	0.376	GT	180×150
135	3×10^{-5}	1.1×10^{-1}	1.10	738.0	769.7	0.335	GT	200×180
136	3×10^{-5}	2.0×10^{-1}	2.43	1380	1391	0.297	WR	240×200
137	3×10^{-5}	3.0×10^{-1}	3.52	1846	1876	0.275	WR	280×250
138	1×10^{-5}	3.6×10^{-3}	0.00099	11.10	—	—	ON	160×100
139	1×10^{-5}	3.7×10^{-3}	0.0022	16.51	—	—	ON	160×100
140	1×10^{-5}	4.0×10^{-3}	0.0050	25.20	—	—	ON	160×100
141	1×10^{-5}	4.44×10^{-3}	0.0074	30.97	—	—	ON	200×130
142	1×10^{-5}	5.1×10^{-3}	0.010	37.05	—	—	MM	200×130
143	1×10^{-5}	7.1×10^{-3}	0.053	107.0	75.23	0.244	GT	224×170
144	1×10^{-5}	1.0×10^{-2}	0.115	182.0	155.5	0.272	GT	224×180
145	1×10^{-5}	1.3×10^{-2}	0.187	266.0	245.0	0.293	GT	240×180
146	1×10^{-5}	2.0×10^{-2}	0.332	441.3	445.9	0.307	GT	280×190
147	1×10^{-5}	3.0×10^{-2}	0.558	688.4	727.5	0.328	GT	280×200
148	1×10^{-5}	4.0×10^{-2}	0.920	973.1	1044	0.299	GT	280×200
149	1×10^{-5}	5.0×10^{-2}	1.39	1227	1421	0.279	GT	320×200
150	1×10^{-5}	6.5×10^{-2}	1.98	1615	1957	0.277	GT	320×200
151	1×10^{-5}	1.0×10^{-1}	3.40	2508	2848	0.262	WR	320×250
152	1×10^{-5}	3.0×10^{-1}	8.21	5087	6366	0.226	WR	360×260
153	3×10^{-6}	1.3×10^{-3}	0.0012	16.61	—	—	ON	180×100

Table 1. For caption see next page.

Scaling behaviour of rotating convection

No.	E	Ra^*	$Nu - 1$	Re_{non}	Re_{zon}	ℓ	Regime	$N_r \times L_{max}$
154	3×10^{-6}	1.5×10^{-3}	0.0052	33.66	—	—	ON	180×100
155	3×10^{-6}	1.7×10^{-3}	0.0070	38.68	—	—	ON	180×120
156	3×10^{-6}	3.0×10^{-3}	0.104	231.8	172.6	0.180	GT	200×180
157	3×10^{-6}	6.0×10^{-3}	0.31	617.6	515.4	0.221	GT	220×200
158	3×10^{-6}	1.0×10^{-2}	0.52	1030	927.0	0.243	GT	280×250
159	3×10^{-6}	1.5×10^{-2}	0.88	1558	1494	0.235	GT	320×280
160	3×10^{-6}	2.0×10^{-2}	1.44	2148	2159	0.221	GT	320×320
161	3×10^{-6}	3.0×10^{-2}	2.65	3171	3707	0.221	GT	320×320
162	3×10^{-6}	4.0×10^{-2}	3.92	4072	5176	0.218	GT	380×380
163	3×10^{-6}	5.0×10^{-2}	5.05	5215	5827	0.200	GT	400×400
164	1×10^{-6}	1.0×10^{-2}	1.478	3191	1868	0.141	GT	380×380
165	1×10^{-6}	2.5×10^{-2}	6.521	9179	10914	0.164	GT	500×450
$Pr = 0.01$								
166	1×10^{-4}	1.79×10^{-1}	0.00032	30.75	—	—	ON	100×60
167	1×10^{-4}	1.83×10^{-1}	0.00044	36.63	—	—	ON	100×60
168	1×10^{-4}	1.9×10^{-1}	0.00062	43.60	—	—	ON	100×80
169	1×10^{-4}	2.0×10^{-1}	0.00082	50.93	—	—	ON	100×80
170	1×10^{-4}	2.35×10^{-1}	0.0020	80.47	—	—	ON	100×80
171	1×10^{-4}	2.5×10^{-1}	0.0025	94.74	—	—	MM	100×80
172	1×10^{-4}	2.8×10^{-1}	0.028	307.6	299.8	0.680	GT	100×100
173	1×10^{-4}	3.2×10^{-1}	0.044	400.8	395.0	0.680	GT	100×100
174	1×10^{-4}	3.6×10^{-1}	0.066	513.1	503.8	0.665	WR	120×120
175	1×10^{-4}	6.0×10^{-1}	0.181	1045	920.4	0.566	WR	160×160
176	1×10^{-4}	1.0×10^0	0.058	2228	1245	0.396	WR	240×240
177	3×10^{-5}	5.5×10^{-2}	0.00021	33.3	—	—	ON	120×90
178	3×10^{-5}	6.0×10^{-2}	0.00072	62.6	—	—	ON	120×100
179	3×10^{-5}	7.0×10^{-2}	0.0017	98.0	—	—	ON	120×110
180	3×10^{-5}	8.0×10^{-2}	0.0022	115.1	—	—	ON	120×120
181	3×10^{-5}	8.4×10^{-2}	0.0031	134.6	—	—	MM	120×120
182	3×10^{-5}	8.5×10^{-2}	0.025	379.5	388.1	0.600	GT	140×127
183	3×10^{-5}	1.2×10^{-1}	0.049	568.7	714.8	0.635	GT	160×150
184	3×10^{-5}	2.0×10^{-1}	0.138	1157	1424	0.560	GT	200×200
185	3×10^{-5}	3.0×10^{-1}	0.296	1928	2194	0.452	WR	240×240
186	1×10^{-5}	2.0×10^{-2}	0.00018	40.67	—	—	ON	160×90
187	1×10^{-5}	2.1×10^{-2}	0.00049	68.87	—	—	ON	160×90
188	1×10^{-5}	2.2×10^{-2}	0.00072	84.81	—	—	ON	160×120
189	1×10^{-5}	2.4×10^{-2}	0.0014	118.0	—	—	ON	160×120
190	1×10^{-5}	2.6×10^{-2}	0.0020	142.0	—	—	ON	160×120
191	1×10^{-5}	2.7×10^{-2}	0.0025	157.0	—	—	MM	180×130
192	1×10^{-5}	2.83×10^{-2}	0.0215	442.7	479.4	0.490	GT	200×130
193	1×10^{-5}	4.0×10^{-2}	0.048	693.7	940.4	0.527	GT	200×130
194	1×10^{-5}	5.8×10^{-2}	0.101	1183	1634	0.529	GT	320×200
195	1×10^{-5}	7.5×10^{-2}	0.150	1612	2247	0.518	GT	320×230
196	1×10^{-5}	1.0×10^{-1}	0.232	2240	3157	0.488	GT	320×230
197	1×10^{-5}	2.0×10^{-1}	0.651	4475	5973	0.355	WR	320×240
198	1×10^{-5}	3.0×10^{-1}	1.15	6396	8146	0.296	WR	360×300
199	1×10^{-5}	5.0×10^{-1}	2.13	9782	9908	0.212	WR	400×360
200	3×10^{-6}	7.0×10^{-3}	0.00025	68.72	—	—	ON	160×100
201	3×10^{-6}	7.2×10^{-3}	0.00055	104.6	—	—	ON	160×100

Table 1. For caption see next page.

No.	E	Ra^*	$Nu - 1$	Re_{non}	Re_{zon}	ℓ	Regime	$N_r \times L_{max}$
202	3×10^{-6}	8.0×10^{-3}	0.00095	131.2	—	—	MM	160×120
203	3×10^{-6}	9.2×10^{-3}	0.0189	564.7	587.4	0.358	GT	200×160
204	3×10^{-6}	1.0×10^{-2}	0.035	757.7	566.9	0.365	GT	240×180
205	3×10^{-6}	2.0×10^{-2}	0.153	2078	2825	0.417	GT	280×260
206	3×10^{-6}	3.0×10^{-2}	0.239	3088	4592	0.434	GT	320×300
207	3×10^{-6}	5.0×10^{-2}	0.427	4782	7837	0.423	GT	320×360
208	3×10^{-6}	7.0×10^{-2}	0.678	6555	11 101	0.385	WR	380×380
209	3×10^{-6}	1.0×10^{-1}	1.04	7444	14 943	0.301	WR	504×480
210	1×10^{-6}	2.5×10^{-2}	0.640	8930	15SSZ717	0.332	GT	500×400
211	1×10^{-6}	4.5×10^{-2}	1.19	12 286	28 600	0.329	GT	640×580

Table 1. Summary of the control parameters and diagnostic quantities of all numerical models in this study. The columns from left to right indicate the following: the Ekman number E , the modified Rayleigh number Ra^* , the Nusselt number $Nu - 1$, the non-zonal Reynolds number Re_{non} , the zonal Reynolds number Re_{zon} , length scale ℓ , the regime corresponding to the flow state, the grid resolution and spherical harmonics of degree l_{max} . Zonal Reynolds number and length scale are only given for the cases in GT and WR regimes.

Appendix B. Critical Rayleigh numbers and wavenumbers

Table 2 lists the critical Rayleigh numbers and wavenumbers of the onset of convection used in this study. Critical values are calculated using the linear onset package of the open-source code MagIC (Wicht 2002), which is freely available at <https://magic-sph.github.io>. We have verified our calculations with previous work. For example, Barik *et al.* (2023) obtained the values $Ra_c = 1.05567 \times 10^7$ and $m_c = 15$ for $E = 1 \times 10^{-5}$ and $Pr = 1$, which is in excellent agreement with our results under the same E and Pr .

Pr	E	Ra_c^*	Ra_c	m_c
0.01	1×10^{-4}	1.695×10^{-1}	1.695×10^5	4
0.01	3×10^{-5}	5.368×10^{-2}	5.964×10^5	5
0.01	1×10^{-5}	1.955×10^{-2}	1.955×10^6	6
0.01	3×10^{-6}	6.759×10^{-3}	7.510×10^6	8
0.01	1×10^{-6}	2.594×10^{-3}	2.594×10^7	12
0.1	1×10^{-4}	2.856×10^{-2}	2.856×10^5	6
0.1	3×10^{-5}	9.351×10^{-3}	1.039×10^6	8
0.1	1×10^{-5}	3.529×10^{-3}	3.529×10^6	11
0.1	3×10^{-6}	1.261×10^{-3}	1.401×10^7	16
0.1	1×10^{-6}	5.102×10^{-4}	5.102×10^7	23
1	1×10^{-4}	6.960×10^{-3}	6.960×10^5	8
1	3×10^{-5}	2.546×10^{-3}	2.829×10^6	11
1	1×10^{-5}	1.056×10^{-3}	1.056×10^7	15
1	3×10^{-6}	4.145×10^{-4}	4.606×10^7	22
7	1×10^{-4}	1.326×10^{-3}	9.282×10^5	8
7	3×10^{-5}	5.183×10^{-4}	4.031×10^6	11
7	1×10^{-5}	2.263×10^{-4}	1.584×10^7	17
7	3×10^{-6}	9.302×10^{-5}	7.235×10^7	25
100	1×10^{-5}	1.731×10^{-5}	1.731×10^7	17

Table 2. Critical modified Rayleigh numbers Ra_c^* , critical Rayleigh numbers Ra_c and critical azimuthal wavenumbers m_c for different Ekman E and Prandtl numbers Pr employed here.

Scaling behaviour of rotating convection

REFERENCES

- ABBATE, J.A. & AURNOU, J.M. 2023 Rotating convective turbulence in moderate to high Prandtl number fluids. *Geophys. Astrophys. Fluid Dyn.* **117** (6), 397–436.
- AUBERT, J., BRITO, D., NATAF, H.-C., CARDIN, P. & MASSON, J.-P. 2001 A systematic experimental study of rapidly rotating spherical convection in water and liquid gallium. *Phys. Earth Planet. Inter.* **128** (1–4), 51–74.
- AURNOU, J.M., BERTIN, V., GRANNAN, A.M., HORN, S. & VOGT, T. 2018 Rotating thermal convection in liquid gallium: multi-modal flow, absent steady columns. *J. Fluid Mech.* **846**, 846–876.
- AURNOU, J.M., CALKINS, M.A., CHENG, J.S., JULIEN, K., KING, E.M., NIEVES, D., SODERLUND, K.M. & STELLMACH, S. 2015 Rotating convective turbulence in earth and planetary cores. *Phys. Earth Planet. Inter.* **246**, 52–71.
- AURNOU, J.M., HEIMPEL, M. & WICHT, J. 2007 The effects of vigorous mixing in a convective model of zonal flow on the ice giants. *Icarus* **190** (1), 110–126.
- AURNOU, J.M., HORN, S. & JULIEN, K. 2020 Connections between nonrotating, slowly rotating, and rapidly rotating turbulent convection transport scalings. *Phys. Rev. Res.* **2** (4), 1–13.
- BAKIK, A., TRIANA, S.A., CALKINS, M., STANLEY, S. & AURNOU, J. 2023 Onset of convection in rotating spherical shells: variations with radius ratio. *Earth Space Sci.* **10** (1), 1–19.
- BARKER, A.J., DEMPSEY, A.M. & LITHWICK, Y. 2014 Theory and simulations of rotating convection. *Astrophys. J.* **791** (1), 13.
- BUSSE, F.H. 1970 Thermal instabilities in rapidly rotating systems. *J. Fluid Mech.* **44**, 441–460.
- BUSSE, F.H. & CARRIGAN, C.R. 1976 Laboratory simulation of thermal convection in rotating planets and stars. *Science* **191** (4222), 81–83.
- BUSSE, F.H. & OR, A.C. 1986 Convection in a rotating cylindrical annulus: thermal rossby waves. *J. Fluid Mech.* **166**, 173–187.
- CARDIN, P. & OLSON, P. 1994 Chaotic thermal convection in a rapidly rotating spherical shell: consequences for flow in the outer core. *Phys. Earth Planet. Inter.* **82**, 235–259.
- CHANDRASEKHAR, S. 1961 *Hydrodynamic and Hydromagnetic Stability*. Oxford University Press.
- CHENG, J.S., AURNOU, J.M., JULIEN, K. & KUNNEN, R.P.J. 2018 A heuristic framework for next-generation models of geostrophic convective turbulence. *Geophys. Astrophys. Fluid Dyn.* **112** (4), 277–300.
- CHRISTENSEN, U.R. 2002 Zonal flow driven by strongly supercritical convection in rotating spherical shells. *J. Fluid Mech.* **470**, 115–133.
- CHRISTENSEN, U.R. & AUBERT, J. 2006 Scaling properties of convection-driven dynamos in rotating spherical shells and application to planetary magnetic fields. *Geophys. J. Intl* **166** (1), 97–114.
- DAVIDSON, P.A. 2014 The dynamics and scaling laws of planetary dynamos driven by inertial waves. *Geophys. J. Intl* **198** (3), 1832–1847.
- DORMY, E., SOWARD, A.M., JONES, C.A., JAULT, D. & CARDIN, P. 2004 The onset of thermal convection in rotating spherical shells. *J. Fluid Mech.* **501**, 43–70.
- ECKE, R.E. & SHISHKINA, O. 2023 Turbulent rotating Rayleigh–Bénard convection. *Annu. Rev. Fluid Mech.* **55**, 603–638.
- GASTINE, T. & AURNOU, J.M. 2023 Latitudinal regionalization of rotating spherical shell convection. *J. Fluid Mech.* **954**, R1.
- GASTINE, T., WICHT, J. & AUBERT, J. 2016 Scaling regimes in spherical shell rotating convection. *J. Fluid Mech.* **808**, 690–732.
- GASTINE, T., WICHT, J. & AURNOU, J.M. 2015 Turbulent Rayleigh–Bénard convection in spherical shells. *J. Fluid Mech.* **778**, 721–764.
- GASTINE, T., YADAV, R.K., MORIN, J., REINERS, A. & WICHT, J. 2013 From solar-like to antisolar differential rotation in cool stars. *Mon. Not. R. Astron. Soc. Lett.* **438** (1), L76–L80.
- GILLET, N. & JONES, C.A. 2006 The quasi-geostrophic model for rapidly rotating spherical convection outside the tangent cylinder. *J. Fluid Mech.* **554**, 343–369.
- GILMAN, P.A. 1977 Nonlinear dynamics of Boussinesq convection in a deep rotating spherical shell-I. *Geophys. Astrophys. Fluid Dyn.* **8** (1), 93–135.
- GUERVILLY, C. & CARDIN, P. 2016 Subcritical convection of liquid metals in a rotating sphere using a quasi-geostrophic model. *J. Fluid Mech.* **808**, 61–89.
- GUERVILLY, C., CARDIN, P. & SCHAEFFER, N. 2019 Turbulent convective length scale in planetary cores. *Nature* **570** (7761), 368–371.
- HAWKINS, E.K., CHENG, J.S., ABBATE, J.A., PILEGARD, T., STELLMACH, S., JULIEN, K. & AURNOU, J.M. 2023 Laboratory models of planetary core-style convective turbulence. *Fluids* **8** (4), 106.

- HORN, S. & SCHMID, P.J. 2017 Prograde, retrograde, and oscillatory modes in rotating Rayleigh–Bénard convection. *J. Fluid Mech.* **831**, 182–211.
- JONES, C.A. 2015 Thermal and compositional convection in the outer core. In *Treatise on Geophysics* (ed. G. Schubert), vol. 8, pp. 115–159. Elsevier.
- JONES, C.A., SOWARD, A.M. & MUSSA, A.I. 2000 The onset of thermal convection in a rapidly rotating sphere. *J. Fluid Mech.* **405** (2000), 157–179.
- JULIEN, K., KNOBLOCH, E., RUBIO, A.M. & VASIL, G.M. 2012 Heat transport in low-Rossby-number Rayleigh–Bénard convection. *Phys. Rev. Lett.* **109** (25), 254503.
- KAPLAN, E.J., SCHAEFFER, N., VIDAL, J. & CARDIN, P. 2017 Subcritical thermal convection of liquid metals in a rapidly rotating sphere. *Phys. Rev. Lett.* **119** (9), 094501.
- KERR, R.M. & HERRING, J.R. 2000 Prandtl number dependence of Nusselt number in direct numerical simulations. *J. Fluid Mech.* **419**, 325–344.
- KERSWELL, R.R. 2002 Elliptical instability. *Annu. Rev. Fluid Mech.* **34** (1), 83–113.
- KING, E.M. & AURNOU, J.M. 2013 Turbulent convection in liquid metal with and without rotation. *Proc. Natl Acad. Sci. USA* **110** (17), 6688–6693.
- KING, E.M. & BUFFETT, B.A. 2013 Flow speeds and length scales in geodynamo models: the role of viscosity. *Earth Planet. Sci. Lett.* **371**, 156–162.
- KING, E.M., STELLMACH, S. & BUFFETT, B. 2013 Scaling behaviour in Rayleigh–Bénard convection with and without rotation. *J. Fluid Mech.* **717**, 449–471.
- KING, E.M., STELLMACH, S., NOIR, J., HANSEN, U. & AURNOU, J.M. 2009 Boundary layer control of rotating convection systems. *Nature* **457** (7227), 301–304.
- LABROSSE, S. 2003 Thermal and magnetic evolution of the earth’s core. *Phys. Earth Planet. Inter.* **140** (1–3), 127–143.
- LAM, K., KONG, D.-L. & ZHANG, K.-K. 2018 Nonlinear thermal inertial waves in rotating fluid spheres. *Geophys. Astrophys. Fluid Dyn.* **112**, 357–374.
- LE BARS, M., CÉBRON, D. & LE GAL, P. 2015 Flows driven by libration, precession, and tides. *Annu. Rev. Fluid Mech.* **47**, 163–193.
- LI, X.-M., HE, J.-D., TIAN, Y., HAO, P. & HUANG, S.-D. 2021 Effects of Prandtl number in quasi-two-dimensional Rayleigh–Bénard convection. *J. Fluid Mech.* **915**, A60.
- LI, Y., FRUEHAN, R.J., LUCAS, J.A. & BELTON, G.R. 2000 The chemical diffusivity of oxygen in liquid iron oxide and a calcium ferrite. *Metall. Trans. B* **31**, 1059–1068.
- LIN, Y. 2021 Triadic resonances driven by thermal convection in a rotating sphere. *J. Fluid Mech.* **909**, R3.
- LIN, Y. & JACKSON, A. 2021 Large-scale vortices and zonal flows in spherical rotating convection. *J. Fluid Mech.* **912**, A46.
- LONG, R.S., MOUND, J.E., DAVIES, C.J. & TOBIAS, S.M. 2020 Scaling behaviour in spherical shell rotating convection with fixed-flux thermal boundary conditions. *J. Fluid Mech.* **889**, A7.
- MIYAGOSHI, T., KAGEYAMA, A. & SATO, T. 2010 Zonal flow formation in the Earth’s core. *Nature* **463** (7282), 793–796.
- OLIVER, T.G., JACOBI, A.S., JULIEN, K. & CALKINS, M.A. 2023 Small scale quasigeostrophic convective turbulence at large Rayleigh number. *Phys. Rev. Fluids* **8** (9), 093502.
- ROBERTS, P.H. 1968 On the thermal instability of a rotating-fluid sphere containing heat sources. *Phil. Trans. R. Soc. Lond.* **263**, 93–117.
- SCHAEFFER, N. 2013 Efficient spherical harmonic transforms aimed at pseudospectral numerical simulations. *Geochem. Geophys. Geosyst.* **14** (3), 751–758.
- SILANO, G., SREENIVASAN, K.R. & VERZICCO, R. 2010 Numerical simulations of Rayleigh–Bénard convection for Prandtl numbers between 10–1 and 104 and Rayleigh numbers between 105 and 109. *J. Fluid Mech.* **662**, 409–446.
- STEVENSON, D.J. 1979 Turbulent thermal convection in the presence of rotation and a magnetic field: a heuristic theory. *Geophys. Astrophys. Fluid Dyn.* **12** (1), 139–169.
- TILGNER, A. & BUSSE, F.H. 1997 Finite-amplitude convection in rotating spherical fluid shells. *J. Fluid Mech.* **332**, 359–376.
- VERZICCO, R. & CAMUSSI, R. 1999 Prandtl number effects in convective turbulence. *J. Fluid Mech.* **383**, 55–73.
- WANG, G.-Q., SANTELLI, L., LOHSE, D., VERZICCO, R. & STEVENS, R.J. 2021 Diffusion-free scaling in rotating spherical Rayleigh–Bénard convection. *Geophys. Res. Lett.* **48** (20), e2021GL095017.
- WICHT, J. 2002 Inner-core conductivity in numerical dynamo simulations. *Phys. Earth Planet. Inter.* **132** (4), 281–302.

Scaling behaviour of rotating convection

- DE WIT, X.M., AGUIRRE GUZMÁN, A.J., MADONIA, M., CHENG, J.S., CLERCX, H.J.H. & KUNNEN, R.P.J. 2020 Turbulent rotating convection confined in a slender cylinder: the sidewall circulation. *Phys. Rev. Fluids* **5** (2), 023502.
- XIA, K.-Q., HUANG, S.-D., XIE, Y.-C. & ZHANG, L. 2023 Tuning heat transport via coherent structure manipulation: recent advances in thermal turbulence. *Natl Sci. Rev.* **10** (6), nwad012.
- YADAV, R.K., GASTINE, T., CHRISTENSEN, U.R., DUARTE, L. & REINERS, A. 2016 Effect of shear and magnetic field on the heat-transfer efficiency of convection in rotating spherical shells. *Geophys. J. Intl* **204** (2), 1120–1133.
- ZHANG, K. 1992 Spiralling columnar convection in rapidly rotating spherical fluid shells. *J. Fluid Mech.* **236**, 535–556.
- ZHANG, K. 1994 On coupling between the Poincaré equation and the heat equation. *J. Fluid Mech.* **268**, 211–229.
- ZHANG, K. & LIAO, X.-H. 2017 *Theory and Modeling of Rotating Fluids: Convection, Inertial Waves and Precession*. Cambridge University Press.
- ZHANG, X., ECKE, R.E & SHISHKINA, O. 2021 Boundary zonal flows in rapidly rotating turbulent thermal convection. *J. Fluid Mech.* **915**, A62.
- ZHANG, X., VAN GILS, D.P.M., HORN, S., WEDI, M., ZWIRNER, L., AHLERS, G., ECKE, R.E, WEISS, S., BODENSCHATZ, E. & SHISHKINA, O. 2020a Boundary zonal flow in rotating turbulent Rayleigh–Bénard convection. *Phys. Rev. Lett.* **124** (8), 084505.
- ZHANG, Y.-J, HOU, M.-Q., LIU, G.-T., ZHANG, C.-W., PRAKAPENKA, V.B, GREENBERG, E., FEI, Y.-W., COHEN, R.E. & LIN, J.-F. 2020b Reconciliation of experiments and theory on transport properties of iron and the geodynamo. *Phys. Rev. Lett.* **125** (7), 078501.
- ZHONG, J.-Q., STEVENS, R.J.A.M., CLERCX, H.J.H., VERZICCO, R., LOHSE, D. & AHLERS, G. 2009 Prandtl-, Rayleigh-, and Rossby-number dependence of heat transport in turbulent rotating Rayleigh–Bénard convection. *Phys. Rev. Lett.* **102** (4), 044502.